



1

Observed versus simulated mountain waves over Scandinavia - improvement by enhanced model resolution?

Johannes Wagner¹, Andreas Dörnbrack¹, Markus Rapp¹, Sonja Gisinger¹, Benedikt Ehard¹, Martina
Bramberger¹, Benjamin Witschas¹, Fernando Chouza¹, Stephan Rahm¹, Christian Mallaun², Gerd Baumgarten³,
5 and Peter Hoor⁴

¹Deutsches Zentrum für Luft- und Raumfahrt, Institut für Physik der Atmosphäre, 82234 Oberpfaffenhofen, Germany

²Deutsches Zentrum für Luft- und Raumfahrt, Flugexperimente, 82234 Oberpfaffenhofen, Germany

³Leibniz Institut für Atmosphären Physik, 18225 Kühlungsborn, Germany

⁴Johannes Gutenberg Universität, Institut für Physik der Atmosphäre, 55099 Mainz, Germany

10 *Correspondence to:* Johannes Wagner (johannes.wagner@dlr.de)

Abstract. Two mountain wave events, which occurred over northern Scandinavia in December 2013 are analysed by means of
airborne observations and global and mesoscale numerical simulations with horizontal mesh sizes of 16 km, 7.2 km, 2.4 km
and 0.8 km. During both events westerly cross-mountain flow induced upward propagating waves in the troposphere and
stratosphere and trapped waves in the lee of the mountains. Despite similar forcing conditions gravity wave breaking occurred
15 during the first event at altitudes between 25 km to 30 km due to weak stratospheric background winds, while waves propagated
to altitudes above 30 km during the second event. In the lower troposphere trapped lee waves with horizontal wavelengths of
15 km to 40 km, which propagated horizontally up to 300 km in the lee of the mountains were observed. Global and mesoscale
simulations with 16 km and 7.2 km grid sizes were not able to simulate the mountain and trapped lee waves properly due



2

J. S. Wagner: GWLCYCLE I campaign

to unresolved mountain peaks. In simulations with 2.4 km and 0.8 km horizontal resolution mountain waves were captured,
20 but exhibited too small amplitudes, too strong decay of trapped waves in the lee of the mountains and too high energy and
momentum fluxes at flight level. Increased fluxes in simulations are caused by reduced downward propagating waves due to
weaker jumps in static stability at the tropopause and reduced gravity wave reflection.

1 Introduction

Internal gravity waves (GWs) are a well known phenomena in the atmosphere and have a strong impact on the exchange of
25 energy and momentum between the troposphere and the middle atmosphere (Fritts and Alexander, 2003). Especially the inter-
action of GWs with the mean flow plays an important role in atmospheric dynamics, as dissipating GWs deposit momentum,
e.g., by wave breaking or radiative damping, which changes the background flow (Eliassen and Palm, 1960). This momentum
deposition affects global circulations like the meridional Brewer Dobson circulation (Holton and Alexander, 2000), or the pe-
riodically changing westerly and easterly winds in the tropic stratosphere, known as the quasi-biennial oscillation (QBO, e.g.,
30 Baldwin et al., 2001).

Due to their importance for atmospheric flows from the boundary layer to the middle atmosphere GWs have been studied
intensively in the past by means of analytical and numerical models (e.g., Queney, 1948; Scorer, 1949; Durran, 1990) and
a large number of field campaigns like the Momentum Budget over the Pyrénées experiment (PYREX, Bougeault et al.,
1990, 1993), the Mesoscale Alpine Programme (MAP, Bougeault et al., 2001), the Terrain-induced Rotor EXperiment (T-
35 REX, Grubišić et al., 2008) or the DEEPWAVE campaign (Fritts et al., 2016). During T-REX, Smith et al. (2008) found that
orographically induced GWs cannot propagate deeply into the stratosphere due to the stratospheric wind minimum, which is
a common climatological feature of the mid-latitudes. However, over Scandinavia numerous studies have demonstrated that
GWs can propagate into the stratosphere probably due to higher wind speeds in the vicinity of the polar vortex and can form
polar stratospheric ice clouds (Dörnbrack et al., 2001; Dörnbrack and Leutbecher, 2001; Dörnbrack et al., 2002) and regions of
40 gravity wave breaking around 30 km altitude (Ehard et al., 2016). The propagation of GWs over New Zealand was studied by
Kaifler et al. (2015), who showed that preferably moderate GW forcing in combination with strong stratospheric winds leads
to deep GW propagation from the troposphere to the middle atmosphere due to smaller wave amplitudes, which reduces the
risk of stratospheric GW breaking.

**J. S. Wagner: GWLCYCLE I campaign****3**

The proper simulation of propagating and breaking GWs with weather and climate models is still a challenge and requires an improved representation of GW-mean-flow-interaction processes in current GW parameterization schemes (Kim et al., 2003). This implies a better understanding of the life cycle of GWs including their sources, their horizontal and vertical propagation and their dissipation in the middle atmosphere.

In order to measure the whole life cycle of GWs from their excitation towards propagation and dissipation, ground-based and airborne observations were conducted over northern Scandinavia during the Gravity Wave Life Cycle I (GW-LCYCLE I) campaign in December 2013. The Scandinavian coastal mountain range together with the wintertime synoptic situation over northern Scandinavia and the proximity to the polar vortex form favourable conditions for the generation of mountain waves (cf. Jiang et al., 2003), which are able to propagate up to mesospheric altitudes. The principal idea of the GW-LCYCLE I campaign was to conduct observations whenever the meteorological conditions favoured mountain wave excitation and vertical wave propagation. In this kind, GW-LCYCLE I was a forerunner experiment to test flight strategies and synergies between the different instruments, which were afterwards applied during the two consecutive gravity wave campaigns DEEPWAVE in New Zealand during austral winter 2014 (Fritts et al., 2016) and GW-LCYCLE II in Scandinavia during winter 2015/2016.

Deep GW-propagation from the troposphere into the middle atmosphere in the lee of the Scandinavian mountains was analysed in Ehard et al. (2016) for two strong mountain wave events during GW-LCYCLE-I. The analysis concentrated on a combination of GW-induced temperature perturbations obtained from mesoscale simulations and ground-based lidar observations, which revealed a continuous GW field from the troposphere to the mesosphere with vertical wavelengths of about 10 km. In the present paper the same two mountain wave events as in Ehard et al. (2016) are analysed with a focus on airborne in-situ and Doppler wind lidar (DWL) measurements. The goal of this paper is to test the ability of a state of the art mesoscale model to simulate three-dimensional GW structures in the upper troposphere and lower stratosphere (UTLS) region and to investigate the influence of horizontal model grid and topography resolution on the simulation results. Of certain interest is the proper simulation of GW induced energy (EF) and momentum fluxes (MF), as these fluxes couple different atmospheric layers and modify the background flow. To our knowledge most of the simulations of observed GW events used horizontal model grid resolutions in the kilometre-scale (e.g., Leutbecher and Volkert, 2000; Doyle et al., 2005; Jiang et al., 2013; Kruse and Smith, 2015) and most studies using airborne observations of GWs were based on one-dimensional in-situ wind measurements (e.g., Smith et al., 2002, 2008). In this study the horizontal model grid resolution is increased to 800 m to resolve single mountain peaks and related vertical winds. Simulation results are compared to troposphere-extending, two-dimensional airborne DWL



4

J. S. Wagner: GWLCYCLE I campaign

measurements along mountain cross sections, which yield an impression of the spatial distribution of GWs. This enables to study the correct representation of small-scale GWs like trapped lee waves in numerical simulations.

The paper is organized as follows: Section 2 gives an overview of the GW-LCYCLE I campaign and the available data sets. In section 3 the numerical simulations and methods, which are used to analyse GWs are presented. The general synoptic
75 situation during the campaign is described in section 4 by means of numerical simulations and GW structures in the UTLS are analysed in section 5. A discussion is given in section 6 and a conclusion is presented in section 7.

2 Campaign and data set overview

2.1 GW-LCYCLE I campaign

The GW-LCYCLE I campaign took place from 2 to 14 December 2013 in Kiruna, northern Sweden (68° N, 20° E; see
80 Fig. 1). The principal observational platform was the Deutsches Zentrum für Luft- und Raumfahrt (DLR) Falcon research aircraft, based at Kiruna airport in the lee of the Scandinavian mountain range. Airborne observations were complemented by radiosonde measurements launched at the windward side of the mountains at Andenes (69° N, 16° E, Norway), at the leeward side at the European Space and Sounding Rocket Range Esrange (68° N, 21° E, Sweden) at Kiruna airport (Sweden) and further downstream at Sodankylä (67° N, 27° E, Finland). In addition, ground-based lidar systems were operated at the
85 Arctic Lidar Observatory for Middle Atmosphere Research (ALOMAR) in Andenes and at Esrange and provided time series of temperature and wind profiles at altitudes between 30 km to 90 km. At Andenes middle atmospheric winds were measured with the Middle Atmosphere Alomar Radar System (MAARSY). The flight strategy during the campaign focused on synoptic situations with strong westerly cross mountain flow, which are favourable for the excitation of mountain waves (Dörnbrack et al., 2001, 2002). The planning of the respective research flights was facilitated by the usage of the Mission Support System
90 (MSS, Rautenhaus et al., 2012), which is a software tool to compute meteorological parameters along virtual flight legs on the basis of numerical weather prediction model output.

Altogether, there were 5 intensive observation periods (IOP) with a total of 6 research flights and 92 radiosoundings (see Table 1). IOP 1 and 5 were characterized by mountain wave events, which were studied with 4 research flights and are investigated in this paper. No research flight could be conducted during a strong mountain wave event on 11 December 2013 (IOP4) as
95 a downslope wind storm with gale force cross winds at Kiruna airport made take-off and landing impossible. The event during IOP2 was dominated by the winter storm "Xaver", which passed over northern Germany (Fenoglio-Marc et al., 2015). This



J. S. Wagner: GWLCYCLE I campaign

5

storm caused mountain and jet-induced GWs over southern Scandinavia and deep propagating convective GWs in a strong, convective cold air outbreak with polar low formation over the Norwegian Sea. Finally, relatively calm conditions prevailed during IOP3, enabling the measurement of polluted air (mainly of SO₂), which was advected towards northern Scandinavia from midlatitudes with sources in the US and China (H. Schlager, 2013, personal communication).

2.2 Airborne observations

The DLR Falcon aircraft was equipped with a downward-looking coherent Doppler wind lidar (DWL) which operates at a wavelength of 2 μm. Within the last years, this lidar system was successfully deployed in several ground-based and airborne field campaigns for instance for measuring aircraft wake vortices (Köpp et al., 2003), aerosol optical properties (Chouza et al., 2015) and the three-dimensional wind field over the Atlantic ocean (Weissmann et al., 2005). Details about the DWL hardware configuration are given by Chouza et al. (2015); Witschas et al. (2016) and details about the retrieval procedure can be found in Smalikho (2003).

During the GW-LCYCLE I campaign, the DWL was operated in scanning or nadir mode aiming to measure the vertical profiles of the three-dimensional wind vector or to measure the vertical wind speed, respectively. While operating in scanning mode, a conical step-and-stare scan around the vertical axes with an off-nadir angle of 20° is performed. 24 line-of-sight (LOS) wind velocities are measured per one scanner revolution and are subsequently used to retrieve the three-dimensional wind vector. Considering 1 s averaging time for each LOS measurement, a total dead time of 6 s for the scanner motion for each scan, and an aircraft speed of about 200 m s⁻¹, the horizontal resolution is about 6 km. During nadir mode operation, the laser beam is pointed to nadir-direction and thus, the measured LOS wind equals the vertical wind speed. In order to increase the signal-to-noise ratio, 4 s are averaged and thus, the horizontal resolution of vertical wind profiles is about 800 m. The vertical resolution for both measurement modes is determined by the laser pulse length and is set to be 100 m.

It has to be mentioned that vertical wind measurements are likely to be contaminated by horizontal wind, which is measured in LOS in case of a not perfectly nadir-pointing laser beam. The separate analysis of raw LOS wind speed profiles during nadir mode along all head- and tailwind flight legs during IOP1 and IOP5 revealed a vertical wind speed offset of -0.46 m s⁻¹ and +0.12 m s⁻¹, respectively. This offset is a result of attitude changes of the aircraft (e.g. pitch and roll angles) due to strong side winds, which induce a deviation of the lidar beam from the nadir pointing direction. In order to correct for that, information about the horizontal wind field and the actual pointing direction (off-nadir angle) are needed. As there are no simultaneous horizontal and vertical wind lidar measurements along the respective flight legs, horizontal wind speeds of the European



6

J. S. Wagner: GWLCYCLE I campaign

Centre for Medium-Range Weather Forecasts (ECMWF) integrated forecast system (IFS) model with a temporal resolution
125 of 1 hour are used as background wind conditions. The actual pointing of the laser beam is calculated for each measurement
by considering the position of both scanner wedges used to steer the laser beam into the atmosphere, and the lidar installation
position which is determined in a separate procedure and which is verified to stay constant during the campaign Witschas et al.
(2016). After correcting for the horizontal wind speed contribution, the mean vertical wind speed for head- and tail wind flight
legs is -0.005 m s^{-1} and -0.078 m s^{-1} , respectively. Thus, the systematic uncertainty of the measured vertical wind speed is
130 less than 10 cm s^{-1} . The statistical uncertainty is determined to be less than 20 cm s^{-1} by analysing the spectral power of the
measured vertical wind speed as described by Frehlich (2001) (not shown). In the following, the corrected vertical wind data
is used for further analysis.

During the GW-LCYCLE I campaign the nadir operating mode was used most frequently, as it was suitable to detect small
scale and often trapped gravity waves over the complex orography. An overview of the flight altitudes and flight legs where
135 the lidar operated in nadir and scanning mode during IOP1 and IOP5 is given in Fig. 2. In this figure the topography height
along the flight legs is represented by the Advanced Spaceborne Thermal Emission and Reflection Radiometer (ASTER) data
set (Schmugge et al., 2003), which has a horizontal resolution of 30 m.

Besides wind lidar observations, in-situ measurements of standard meteorological parameters were measured at flight level
during all research flights with a time resolution of 1 s. The measurement of in-situ 3-dimensional wind is described in Mallaun
140 et al. (2015) and the verification of airborne pressure measurements in Giez et al. (2016). Trace gas measurements were
performed at flight level with the water vapour analyser (WARAN) hygrometer (Groß et al., 2014) and a mass spectrometer for
the trace gases water vapour and SO_2 , respectively. The University of Mainz Airborne Quantum Cascade Laser-spectrometer
(UMAQS; Müller et al., 2015) was applied to measure mixing ratios of the passive tracers N_2O and CO , which are chemically
inert in the UTLS. The transition from constant tropospheric ($327.5 \text{ ppbv} \pm 0.9 \text{ ppbv}$) to decreasing stratospheric N_2O mixing
145 ratios allows for the determination of the chemical tropopause, which was defined by mixing ratios of 326.6 ppbv during
GW-LCYCLE I. The main objective of trace gas measurements was to detect GW induced vertical mixing processes in the
tropopause region. This is, however, not examined in this study.

2.3 Ground based observations

Airborne measurements were complemented by ground based meteorological observations. During the five IOPs a total of 92
150 radiosondes were released both on the wind and leeward side of the mountain range at Andenes (Norway), Esrange (Sweden),



J. S. Wagner: GWLCYCLE I campaign

7

Kiruna (Sweden) and Sodankylä (Finland). Depending on wind conditions the sondes drifted up to 390 km horizontally and reached altitudes of more than 30 km in most cases. This dataset allows to study tropospheric GWs and their propagation through the tropopause into the lower stratosphere. In addition to radiosonde observations, the Esrange Rayleigh lidar provided 130 hours of temperature profiles of the middle atmosphere between altitudes of 30 km to 65 km. The lidar measurements were conducted during the period of 24 November to 14 December 2013. The analysis of the lidar and radiosonde data in combination with mesoscale numerical modeling is described in Ehard et al. (2016).

3 Numerical models and analysis methods for GWs

3.1 Real-case simulations

Mesoscale numerical simulations of the two mountain wave events IOP1 and IOP5 are performed with the Weather Research and Forecasting (WRF) model, version 3.7 (Skamarock et al., 2008). Up to three nested domains (D1, D2, and D3) with horizontal resolutions of 7.2 km, 2.4 km and 0.8 km (see Fig. 1) are used. For the two coarse domains 138 terrain following levels with stretched level distances of 80 m near the surface and 300 m in the stratosphere are used and the model top is set to 2 hPa (about 39 km altitude). For the innermost domain only 78 vertical levels are applied and the model top is set to 50 hPa (about 20 km altitude) due to limitations in computational resources. At the model top a 7 km thick Rayleigh damping layer (Klemp et al., 2008) is applied to prevent wave reflection. Physical parameterizations contain the Rapid Radiative Transfer Model longwave scheme (Mlawer et al., 1997), the Goddard shortwave scheme (Chou and Suarez, 1994), the Mellor-Yamada-Nakanishi-Niino boundary layer scheme (Nakanishi and Niino, 2009), the Noah land surface model (Chen and Dudhia, 2001), the WRF single-moment 6-class microphysics scheme (WSM6; Hong and Lim, 2006) and the Kain-Fritsch cumulus parameterization scheme (Kain and Fritsch, 1990). The latter is switched off for the innermost domain. Horizontal diffusion (WRF parameter `diff_opt`) was not applied in the two innermost domains to increase GW amplitudes in vertical wind fields. The initial and boundary conditions are supplied by ECMWF (T1279 L137, cycle 40r1) operational analyses on 137 model levels with a temporal resolution of 6 hours. WRF and ECMWF fields are interpolated in space and time on aircraft flight tracks to compare with observational data. For this purpose, a temporal output interval of 5 minutes is used in the WRF simulations. For ECMWF a 1 hourly output interval is realized by performing short-term forecasts with the ECMWF IFS. In order to compute GW induced energy and momentum fluxes the diagnostic filtering method of Kruse and Smith (2015) is applied to WRF output.



8

J. S. Wagner: GWLCYCLE I campaign

In addition to the WRF control simulation (CTRL) three sensitivity runs are performed (see Table 2): in the NOTOPO and OCEAN simulations the topography height is set to zero everywhere in the domain. In addition, the landuse type has properties of a water surface with a roughness length of 0.0001 m everywhere in the domain in the OCEAN runs. The NOTOPO and OCEAN simulations aim to define an atmospheric background state without mountain waves and to investigate the influence of changing surface roughnesses (transition from an ocean to a land surface) on GW excitation. In the SMTOPO simulations the two innermost domains use a smoothed topography, which is the same as in the outermost (D1) model domain. This is done to analyse the effect of unresolved topography on GW structures in a high resolution model.

All WRF topographies are based on the Global 30 Arc-Second Elevation (GTOPO30) digital elevation model with a maximum horizontal resolution of about 1 km, while the ASTER data set with a horizontal resolution of 30 m is used as reference topography. Figure 3 illustrates the different representation of the Scandinavian mountain range in the single model runs by means of two example flight legs during IOP1 and IOP5. The innermost WRF domains D2 and D3 ($\Delta x = 2.4$ km and 0.8 km) resolve the single mountain peaks very well in terms of amplitude and horizontal wavelength (note the local peak in the power spectra at about 20 km). Domain D1 and the ECMWF model do not capture the fine scale mountain peaks and represent the topography as a single, smooth mountain ridge. The influence of topography resolution on the simulated vertical wind field is investigated in section 5.

3.2 Idealised simulations

To investigate the relation between EF and MF in situations with hydrostatic and trapped waves, 2-dimensional idealised WRF simulations are performed. GWs are generated by flow over an isolated Witch of Agnesi mountain with a mountain half-width of 10 km and a mountain height of 200 m. For the hydrostatic mountain wave case (HYDRO; see Table 2) a constant horizontal wind speed of 10 m s^{-1} and a Brunt-Vaisala frequency N of 0.01 s^{-1} is used. The trapped lee wave case (TRAPPED) is initialised according to profile 2 of Hills et al. (2016, their Fig. 2) with a constant horizontal wind speed of 20 m s^{-1} and a three layer atmosphere with a stable 2.5 km deep planetary boundary layer (PBL) with $N = 0.016 \text{ s}^{-1}$, a 7.5 km deep troposphere with $N = 0.0045 \text{ s}^{-1}$ and a stratosphere above 10 km height with $N = 0.02 \text{ s}^{-1}$. Both simulations are run for 10 h and apply a horizontal mesh size of 1 km and a model top at 30 km.



J. S. Wagner: GWLCYCLE I campaign

9

3.3 Computation of fluxes and diagnostic variables

The computation of EF and MF at flight level according to the method of Smith et al. (2008) provides information about GWs in the UTLS region and is applied for both observations and simulations in this study. The leg-integrated fluxes are computed by the formulas:

$$205 \quad MF_x = \frac{\bar{\rho}}{L} \int w' u' dx, \quad (1)$$

$$MF_y = \frac{\bar{\rho}}{L} \int w' v' dx, \quad (2)$$

and

$$EF = \frac{1}{L} \int w' p' dx, \quad (3)$$

210 with zonal and meridional momentum flux MF_x and MF_y , GW induced perturbations of zonal wind u' , meridional wind v' , vertical wind w' , pressure p' , leg averaged density $\bar{\rho}$ and leg length L . Momentum and energy fluxes are connected by the Eliassen-Palm relation (Eliassen and Palm, 1960):

$$EF = -U \cdot MF, \quad (4)$$

with

$$215 \quad MF = u \cdot MF_x + v \cdot MF_y, \quad (5)$$

with leg averaged zonal, meridional and total horizontal wind speed u , v and U , respectively. The wind and pressure perturbations u' , v' , w' and p' are computed by subtracting linear regressions from full wind and pressure fields along flight legs. For pressure, a hydrostatic correction is applied in advance of computing the pressure perturbations as described in (Smith et al., 2008).

220 Further diagnostic variables are used in this study to describe flow and GW characteristics. The gradient Richardson number is a measure to differentiate between laminar and turbulent flows and is defined as $Ri = N^2 \left(\frac{dU}{dz} \right)^{-2}$ with Brunt-Vaisala frequency N . Typically a flow is turbulent for $Ri < 0.25$.

The Scorer parameter $l = \sqrt{N^2/U^2 - \frac{1}{U} \frac{d^2U}{dz^2}}$ is a quantity from linear wave theory (Scorer, 1949) and is used to distinguish between different wave regimes, like evanescent and vertically propagating waves. Trapped lee waves occur in layers where l



10

J. S. Wagner: GWLCYCLE I campaign

225 is decreasing with height, which means that only waves with horizontal wave numbers smaller than l can propagate vertically.

In this study the curvature term is neglected for simplification and l is computed as $l = \sqrt{N^2/U^2}$.

The reflection of trapped waves at the tropopause depends on the jump in static stability between the troposphere and the stratosphere. It can be expressed according to Keller (1994) by the reflection coefficient r for hydrostatic waves in case of large Richardson numbers by $r \approx \frac{N_2 - N_1}{N_2 + N_1}$ with stratospheric and tropospheric Brunt-Vaisala frequencies N_2 and N_1 .

230 4 Synoptic situation during IOP1 and IOP5 from simulations

Meteorological situations favourable for the generation of mountain waves occurred at the beginning (IOP1) and end (IOP5) of the GW-LCYCLE I campaign (see Table 1). The meteorological condition during IOP1 (3 December 2013) was dominated by a strong synoptic low pressure system, which was located over the northern Norwegian Sea and travelled eastwards from the coast of Greenland towards northern Norway (see Fig. 4). At the tropopause level a strong westerly jet moved southwards during IOP1. The cross mountain flow caused GW excitation and related vertical energy fluxes in the middle troposphere along the whole Scandinavian mountain range with largest fluxes occurring over the Kiruna region (Fig. 4(c)).

The GW event during IOP1 can be divided into three phases, which are visible in the time height sections for horizontal wind speed, gradient Richardson number, vertical energy flux and Scorer parameter at the location Abisko (68° N, 19° E; Fig. 5 (a) to (d)), which is situated in the centre of the mountain range between Andenes and Kiruna (see the dots in Fig. 4). The first GW phase (P1) was dominated by moderate westerly cross mountain flow at low levels (30 m s^{-1} at 850 hPa) within the warm air sector of the synoptic low (not shown) and moderate vertical energy fluxes. The second phase (P2) was characterized by weak low level winds (15 m s^{-1}) and low GW activity due to calm conditions after the passage of a cold front. At upper levels the tropopause jet was located directly over the Kiruna region, which caused an increase of horizontal wind speed and decrease of the Scorer parameter l with height. This induced the formation of trapped lee waves in the lower troposphere (not shown). At about 6 UTC on 3 December the third phase (P3) started when low level winds intensified due to the approaching low pressure system (cf. Fig. 4). During this phase atmospheric background conditions were less ideal for the formation of trapped waves in the lower troposphere compared to P2. GW excitation stopped at about 3 UTC on 4 December when the low pressure system moved further east. The two research flights of IOP1 took place during phase P3 (see Fig. 5).

250 During IOP5 (13 December 2013) the situation was less complex as northern Scandinavia was located below a strong and quasi stationary northwesterly tropopause jet (Fig. 4(e)) in polar air masses far north of the polar front (not shown). The low



J. S. Wagner: GWLCYCLE I campaign

11

level forcing was weaker than during IOP1 and dominated by a polar low like short wave trough, which developed in a cold air outbreak south of Svalbard reaching the Norwegian coast at about 6 UTC on 13 December. Mountain wave generation was restricted to northern Scandinavia (Fig. 4(f)) and started at about 0 UTC on 13 December and stopped immediately when the polar low dissolved at about 17 UTC on 13 December (Fig. 5(e) and (f)). Due to the presence of the strong tropopause jet, 255 trapped waves could develop at an altitude range between 2 km and 10 km (see the decreasing values of Scorer parameter with height in these levels between 6 UTC to about 16 UTC, Fig. 5(h)).

Despite similar cross mountain flow during both IOPs, the vertical wave propagation in the stratosphere was different. While during IOP5 continuously propagating GWs developed, GW breaking occurred at altitudes between about 25 km to 30 km during IOP1, which is visible from convective overturning, reduced Richardson numbers Ri , increased nonlinearity ratios 260 (NLR, Kruse and Smith, 2015) and decreasing energy fluxes in this altitude range during phase P3 in Fig. 5. This turbulent region was also measured by radiosondes started at Andenes, which measured strongly reduced horizontal wind speeds (smaller than 10 m s^{-1}) between an altitude of 25 km to 30 km (not shown).

To investigate the reason for different GW structures in the stratosphere the NOTOPO and OCEAN simulations are analysed. Wind speeds in these simulations can be regarded as atmospheric background state without perturbations due to mountain 265 waves. The solid lines in Fig 6 show time series of horizontal wind speeds averaged between 25 km to 30 km at Abisko obtained from the NOTOPO and OCEAN simulation and reveal about 10 m s^{-1} lower wind speeds during IOP1 compared to IOP5. The grey shading in Fig. 6 indicates maximum and minimum GW-induced wind speed perturbations obtained by subtracting OCEAN from CTRL run fields. During IOP1 weaker background winds and stronger wind perturbations generated regions with winds below 10 m s^{-1} , which favour local mountain wave breaking due to critical level dissipation. During 270 IOP5, however, wind speeds stayed above 20 m s^{-1} at this altitude range and enabled wave propagation to altitudes above 30 km (cf. Fig. 5). In addition, the comparison of NOTOPO and OCEAN simulations shows nearly no difference in horizontal wind speeds. This indicates that GWs are not generated by changes in roughness lengths in the NOTOPO run, when the flow passes over the ocean and reaches the land surface, as NOTOPO (water and land surfaces) and OCEAN (only water surfaces) simulations generate the same wind field.

275 Beside the GW evolution in the lower and middle stratosphere the focus of this study is on GW structures in the UTLS, as this part of the atmosphere was observed by airborne measurements. Figure 7 shows snapshots of vertical velocity at 500 hPa at 12 UTC on 03 and 13 December 2013 taken from the CTRL D3 simulations. This represents the situation in between of the two respective research flights during IOP1 and IOP5. Small-scale up- and downdrafts over the mountains indicate the



12

J. S. Wagner: GWLCYCLE I campaign

existence of GWs. During both IOPs waves are propagating horizontally in the lee of the mountain range and over the ocean
280 behind the Lofoten islands. The trapped lee wave signatures were weaker during IOP1 due to an increasing Scorer parameter
with height at this altitude (cf. Fig. 5).

In Fig. 8 CTRL upstream profiles of horizontal wind speed averaged over a region between 69°N to 70°N and 10°E to
15°E (see small black boxes over the ocean in Fig. 7) indicate relatively strong and constant horizontal wind speeds between
25 m s⁻¹ to 30 m s⁻¹ in the troposphere during IOP1. In contrast, a strong increase in wind speed from 10 m s⁻¹ near the
285 surface to 50 m s⁻¹ at the tropopause existed during IOP5. Profiles of the Scorer parameter show favourable conditions for
trapped lee waves during IOP5 with decreasing values of l with height between 2 km and 4 km and between 5 km and 8 km
altitude. This means that only waves with horizontal wavelengths larger than about 30 km were able to propagate vertically into
the stratosphere in the model. Regionally averaged profiles over the mountain region between 67°N to 69°N and 15°E to 25°E
(see large black box in Fig. 7) of vertical energy fluxes show upward propagating waves during both IOPs with a maximum in
290 the jetstream region during IOP5. Local minima of vertical energy fluxes below 5 km altitude hint towards reflected up- and
downward propagating lee waves and cancellation of vertical energy fluxes, especially during IOP5. During phase P3 of IOP1
the conditions for trapped lee waves were less ideal due to stronger low level winds and increasing Scorer parameter above
4 km altitude.

5 Observed versus simulated GWs in the UTLS region

295 5.1 Sensitivity of simulated GWs to grid and topography resolution

To give an impression of observed and simulated wave structures, vertical wind speeds along flight leg 2 of the respective first
research flights during IOP1 and IOP5 are shown in Fig. 9 and 10. The airborne lidar and in-situ measurements show regions
of alternating up- and downward motions along the whole flight leg with amplitudes of 2 m s⁻¹ to 4 m s⁻¹ and nearly vertical
phase lines. The strongest signals occur directly over the mountains and extend horizontally up to 300 km eastward in the lee
300 of the mountain range (Fig. 9 and 10 (a), (b)). There are also wave structures visible on the upstream side over the ocean, which
intensify when the flow passes over islands and the main mountain range.

The simulated vertical wind field depends strongly on the grid and topography resolution. As the CTRL D1 run does not
resolve single mountain peaks (cf. Fig. 3), the vertical wind field is very smooth and nearly no trapped waves are visible. With
a horizontal resolution of 2.4 km and 0.8 km the mountain peaks and vertical winds are resolved in the CTRL D2 and D3



J. S. Wagner: GWLCYCLE I campaign

13

305 simulations, however, with weaker amplitudes compared to the observations. Isentropes show upward propagating waves with slightly upstream tilted phase lines over the mountains and vertical phase lines of trapped waves in the lee of the mountains in the CTRL D2 and D3 simulation. Nearly vertical phase lines of propagating waves over the mountains were caused by strong wind shear especially during IOP5 (see Fig. 8(a) and (d)). In the stratosphere, above the tropopause jet, upward propagating waves with stronger phase tilts are visible in the CTRL D2 and D3 runs. The combination of high model resolution with
310 smoothed topography in the SMTPO D3 simulation (Fig. 9 and 10 (i), (j)) results in a vertical wind field, which is very similar to the coarse resolution CTRL D1 run (Fig. 9 and 10 (c), (d)). This shows that a proper representation of single mountain peaks is necessary for the simulation of realistic vertical winds.

In the lee of the mountains lidar and in-situ observations show trapped wave structures along the whole flight leg. These waves are also visible in the CTRL D2 and D3 simulations, but reveal a stronger decay of wave amplitudes compared to
315 observations. It is supposed that trapped lee waves are damped in the model by leakage of wave energy into the stratosphere due to reduced wave reflection at the tropopause (Hills et al., 2016).

On the upstream side all simulations reveal very smooth vertical winds in contrast to lidar and in-situ observations. This can be explained by missing perturbations, e.g., due to convective GWs. It is assumed that the east-west extent of the WRF modelling domains (see Fig. 1) would have to be much larger to allow the development of convection induced GWs in the
320 westerly flow over the ocean. This was, however, not possible in this study due to limitations in computational resources. In addition, missing wave structures in the ECMWF analysis data, which are used as initial and boundary conditions for the WRF model, contribute to the smooth upstream vertical wind fields.

The relation between topography resolution and simulated vertical wind field is demonstrated by comparing Fig. 3 and Fig. 11. The latter shows vertical wind speeds at flight level along two example flight legs during IOP1 and IOP5 (the same
325 legs as in Fig. 3, 9 and 10). The power spectra of observed vertical velocity reveal dominant wavelengths between 15 km to 40 km. Similar wavelengths were obtained from the corresponding topographies in Fig. 3, which illustrates the linkage between single mountain peaks and up- and downdrafts. The CTRL D2 and D3 runs partially reproduce these wavelengths, however, with significantly smaller amplitudes, while they cannot be resolved by CTRL D1, SMTPO and ECMWF.

5.2 Observed versus simulated energy and momentum fluxes

330 The airborne observations during IOP1 and IOP5 enable to study the correct simulation of GW induced energy (EF) and momentum (MF) fluxes in the UTLS. EF and MF at flight level are computed according to the method of Smith et al. (2008,



14

J. S. Wagner: GWLCYCLE I campaign

see section 3.3) and are shown in Fig. 12. During both IOP1 and IOP5 the linear Eliassen-Palm relation between EF and MF is satisfied well in in-situ observations and WRF simulations and indicates upward propagating mountain waves. Note that only data directly above the mountains (cf. black dotted lines in Fig. 2) are used for flux computations to avoid nonlinearity effects in observational data in upstream regions. For ECMWF the relatively short lengths of the mountain legs cause inadequate linear Eliassen-Palm relations. Along complete legs (cf. black dashed lines in Fig. 2) the linear relation is achieved well for ECMWF (not shown).

Surprisingly, energy and momentum fluxes are significantly larger in the WRF model during both IOPs compared to in-situ observations (also for complete flight legs; not shown) in spite of smaller wave amplitudes (cf., Fig. 9 and 10). To study the reason for increased fluxes in the model, energy and momentum fluxes are plotted pointwise for all flight legs during IOP1 and IOP5 in Fig. 13 (a) and (c). As in Fig. 12 the linear relation between EF and MF is satisfied well for observations and simulations. Observations indicate both positive and negative values for EF and MF, while positive EF and negative MF dominate in the simulations. This can be explained by weaker trapped waves (see Fig. 9 and 10) and related weaker downward wave reflection in the simulations.

To test this hypothesis energy and momentum fluxes are computed for the idealised 2-dimensional hydrostatic (HYDRO) and trapped lee wave (TRAPPED) cases (see Table 2). Figure 14 shows EF and MF for the HDYDRO and TRAPPED simulations after 10 h of integration. In the HDYDRO case the perturbations w' and u' and w' and p' are in phase (not shown) and positive EF and negative MF occur over the mountain, while there are also regions of negative EF and positive MF on the upstream and downstream side. A similar figure is given for the analytic Queney solution of hydrostatic waves in Kruse and Smith (2015). The pointwise correlation between EF and MF (Fig. 14b) shows that positive EF and negative MF dominate due to upward propagating waves.

In the TRAPPED case the phase shift between w' and u' and between w' and p' is 90° (not shown). Alternating positive and negative EF and MF are visible in the PBL and in the troposphere in Fig. 14 (c). The scatter plot of EF and MF in Fig. 14(d) shows an equal distribution of positive and negative EF and MF in the PBL and in the troposphere due to reflected up- and downward propagating waves. In the stratosphere positive EF and negative MF values dominate due to upward propagating waves by leakage of wave energy through the tropopause.

A comparison of the scatter plots in Fig. 13 and Fig. 14 shows similarities between the idealised HYDRO and real-case CTRL simulations and between the TRAPPED simulation and observational data. This means that hydrostatic waves dominated and trapped waves and downward wave reflection were underestimated in the CTRL simulations, which leads to increased leg-



J. S. Wagner: GWLCYCLE I campaign

15

360 integrated fluxes (Fig. 12). This is in agreement with too strong decay of simulated trapped waves in Fig. 9 and 10 by leakage of wave energy into the stratosphere (Durran et al., 2015; Hills et al., 2016).

Hydrostatic waves can also be distinguished from trapped waves by computing the linear correlation between the perturbations $w'p'$, $w'u'$ and $w'v'$. Due to the phase shift of 90° , low correlations of 0.07 for $w'p'$ and -0.10 for $(w'u')$ were determined in the idealised TRAPPED simulation, while high values of 0.75 ($w'p'$) and -0.88 ($w'u'$) were calculated for the HYDRO case. 365 Figure 13 (b) and (d) show correlations for real-case simulations and observed GW perturbations during IOP1 and IOP5. All simulations show high values due to dominating hydrostatic waves, whereas observed correlations are significantly smaller with values below 0.2. During IOP1 (Fig. 13 (b)) a clear trend from high to low correlations is visible when increasing the model resolution due to an improved representation of trapped waves.

Beside downward wave reflection, observed correlations between $w'p'$, $w'u'$ and $w'v'$ and respective EF and MF could also 370 be smaller compared to simulations due to small-scale, non-linear (i.e. turbulent) perturbations, which are superimposed to GW induced disturbances in observations but missing in CTRL and ECMWF simulations. To test the impact of these small-scale disturbances on EF and MF, in-situ data were smoothed by eliminating waves with horizontal wavelengths smaller than 15 km (In-situSM). This threshold was chosen, as wavelengths of 15 km and larger were well resolved in CTRL D2 and D3 simulations (see Fig. 11) and thus, signals of In-situSM and CTRL D2 and D3 are comparable. The smoothing does not 375 influence EF and MF, as can be seen when comparing the original (In-situ) and filtered (In-situSM) fluxes in Fig. 12 and correlations of GW induced perturbations in Fig. 13 (b) and (d) are only slightly increased for In-situSM. This indicates that small-scale (< 15 km) perturbations do not contribute significantly to EF and MF, which means that increased simulated EF and MF are caused by underestimated wave reflection and not by unresolved small-scale disturbances.

According to Keller (1994) the reflection (and correspondingly the leakage) of trapped waves depends on the jump in static 380 stability at the tropopause and can be expressed by the reflection coefficient r (see section 3.3). Figure 15 shows observed and CTRL D2 vertical profiles of static stability obtained from soundings started at Andenes during both IOPs. It is visible that for nearly all profiles the change in stability at the tropopause is more distinct for observations than for simulations. This results in higher observed reflectivity coefficients r and explains the intensified observed downward wave propagation and correspondingly increased negative energy fluxes compared to simulations.



385 **5.3 Model verification**

In order to verify the model results of the previous sections, simulations are compared quantitatively to in-situ and lidar observations. Figure 16 shows correlations of airborne in-situ and lidar measurements with numerical models for potential temperature, wind direction and vertical and horizontal wind speed for all legs during IOP1 and IOP5. Except vertical wind speed all variables are captured well by both the WRF and ECMWF model with similar correlation coefficients and root mean square errors (RMSE) independently of the horizontal resolution. This good agreement can be explained as fields of potential temperature and horizontal wind speed are principally dominated by large-scale waves. Vertical winds on the other hand reflect small-scale up- and downdrafts, which are linked to single mountain peaks (cf. Fig. 3 and Fig. 11) and may be shifted slightly in space and time in the models, which complicates a pointwise comparison with measurements. A separation of correlation coefficients for both IOPs is listed in Table 3 and indicates that IOP5 was captured better by the models than IOP1 probably due to the less complex meteorological situation (see section 4).

To verify vertical velocities in a different way, the distribution of lidar, WRF and ECMWF vertical winds are computed. Figure 17 (a) shows the distribution of vertical velocity along all flight legs during both IOP1 and IOP5, where the lidar was operating in nadir pointing mode. The observed lidar data exhibit a broad distribution with large wave amplitudes of maximum up- and downdrafts of 5.0 m s^{-1} and -8.1 m s^{-1} . The CTRL D3, D2, D1 and especially the ECMWF model simulate narrower distributions with maximum and minimum vertical winds of 8.25 m s^{-1} and -8.23 m s^{-1} , 4.7 m s^{-1} and -5.3 m s^{-1} , 0.99 m s^{-1} and -0.95 m s^{-1} and 0.46 m s^{-1} and -0.35 m s^{-1} , respectively.

Figure 17 (b) shows the relation between the mean vertical velocity amplitude along all nadir pointing lidar flight legs and the horizontal model resolution (for lidar data a resolution of 800 m was applied; see section 2.2). The largest improvement in simulating vertical velocities is achieved by reducing the horizontal mesh size from 7.2 km to 2.4 km (CTRL D1 and CTRL D2) due to the more realistic topography representation in CTRL D2 (see Fig. 3). The importance of a properly resolved topography for the simulated vertical wind field is indicated by the SMTPOPO runs, which show nearly the same amplitudes as the CTRL D1 run. Equal values of the NOTOPO and OCEAN simulations indicate that GWs are not induced by a change in roughness length when the flow passes the coast line in the NOTOPO simulation.



J. S. Wagner: GWLCYCLE I campaign

17

6 Discussion

410 The comparison of simulations with airborne observations of the two mountain wave events revealed the following results for GWs in the UTLS region:

- Horizontal wind speed and temperature are captured by both global and mesoscale simulations independently of the horizontal resolution, as perturbations of these fields are dominated by large-scale GWs.
- Airborne observations of vertical velocity show small-scale up- and downdrafts with horizontal wavelengths between 15
415 to 40 km. These waves are linked to single mountain peaks with a similar wavelength range. The realistic simulation of vertical winds implies a properly resolved topography, which is satisfied over Scandinavia for horizontal mesh sizes smaller than 2.4 km.
- In the troposphere trapped lee waves existed in observations and in simulations with grid distances smaller than 2.4 km. Compared to observations, simulated vertical velocity amplitudes were too small and trapped waves decayed too much
420 due to reduced jumps of static stability at the tropopause and correspondingly reduced wave reflection. This means that upward propagating hydrostatic waves dominated in the simulations, which lead to increased flight leg-integrated EF and MF. This was qualitatively confirmed by idealised simulations, as pointwise distributions of EF and MF of observations and real-case simulations were similar to distributions of idealised trapped and hydrostatic waves, respectively.
- GW induced vertical wind and pressure perturbations w' and p' are in phase for hydrostatic waves and are shifted by 90°
425 for trapped waves. This yields higher linear correlations between these perturbations and larger EF and MF for hydrostatic waves compared to trapped waves. Significantly higher correlations between $w'p'$, $w'u'$ and $w'v'$ were found in real-case simulations compared to observations due to weaker simulated wave reflection at the tropopause.
- In observations turbulent perturbations are superimposed to GW induced disturbances. The non-linearity of these disturbances could decrease EF and MF in observations compared to simulations, where these perturbations are missing.
430 Low-pass filtering of observational data by eliminating waves with horizontal wavelengths smaller than 15 km did not influence the resulting EF and MF. This indicates that increased EF and MF in simulations are caused by attenuated wave reflection and not by missing turbulent perturbations.



7 Conclusions

In this study two mountain wave events were analysed, which occurred during the GW-LCYCLE I field campaign in December
435 2013 by means of airborne observations and numerical simulations. During the campaign the DLR Falcon aircraft was stationed
at Kiruna airport to measure GWs above northern Scandinavia. Airborne in-situ and lidar observations were accompanied by
ground-based lidar, radar and radiosonde observations on the wind- and leeward side of the Scandinavian mountain range.

Two mountain wave events IOP1 and IOP5 were observed by 4 cross-mountain research flights, which provided lidar
measurements of horizontal and vertical wind speed and in-situ observations of standard meteorological parameters. Sev-
440 eral mesoscale simulations with different horizontal resolutions, smoothed topography and flat surfaces were performed to
analyse the meteorological situation and to test the ability of a state of the art mesoscale model to capture small-scale GWs. In
contrast to Ehard et al. (2016), who analysed the same GW cases with a focus on waves in the middle atmosphere, this paper
concentrated on GW structures in the tropo- and lower stratosphere, as these atmospheric levels were observed by airborne
measurements.

445 Both IOPs were characterized by westerly cross mountain flow with upward propagating waves in the stratosphere and GW
breaking between 25 km to 30 km altitude during IOP1. In the lower troposphere trapped lee waves developed with horizontal
wavelengths between 15 km to 40 km. As these waves were linked to mountain peaks with wavelengths of the same order, the
proper simulation of tropospheric wave structures depended strongly on the chosen topography resolution. Tropospheric GWs
were not properly simulated in runs with high model grid resolutions and smoothed topography (SMTOP) and in simulations
450 with mesh sizes larger than 2.4 km (CTRL D1 and ECMWF).

The comparison of simulated and measured vertical wind speeds showed too small wave amplitudes, too strong decay of
trapped waves in the lee of the mountains and too high leg integrated energy and momentum fluxes at flight level in mesoscale
simulations in spite of high horizontal resolutions of up to 800 m. The pointwise comparison of energy and momentum fluxes
between observations and simulations showed weaker downward propagating waves in the models. This indicates that leak-
455 age of wave energy at the tropopause was present in the WRF simulations, which intensifies upward propagating waves in
the stratosphere. An explanation for increased leakage are weaker jumps of static stability at the tropopause in simulations
compared to stability profiles obtained from soundings. This reduces the wave reflectivity and the downward propagation of
waves. Additional sensitivity runs with significantly increased vertical grid resolution in the tropopause region might improve
downward wave reflection. Further sources of errors concerning the simulated GWs can be found in upstream vertical wind



J. S. Wagner: GWLCYCLE I campaign

19

460 fields, which are very smooth in ECMWF and WRF simulations, but strongly disturbed in observations. WRF runs driven by
ECMWF ensemble members could be a first step to investigate the role of upstream variability of meteorological fields on the
resulting GW structures.

Acknowledgements. This study was funded by the German ministry of research in the framework of the project "Role of the middle at-
mosphere in climate" (ROMIC) under Grant 01LG1206A. Mesoscale simulations were performed at the Leibniz Institute for Atmospheric
465 Physics (IAP) in Kühlungsborn, Germany. The code to compute the diagnostic GW energy and momentum fluxes was kindly provided by
Chris Kruse, Yale University.

References

- Baldwin, M. P. et al.: The quasi-biennial oscillation, *Rev. Geophys.*, 39, 179–229, doi:10.1029/1999RG000073, 2001.
- Bougeault, P., Jansa Clar, A., Benech, B., Carissimo, B., Pelon, J., and Richard, E.: Momentum budget over the Pyrénées: The PYREX
470 experiment, *Bull. Amer. Meteor. Soc.*, 71, 806–818, doi:10.1175/1520-0477(1990)071<0806:MBOTPT>2.0.CO;2, 1990.
- Bougeault, P., Binder, P., Buzzi, A., Dirks, R., Kuettner, J., Houze, R., Smith, R. B., Steinacker, R., and Volkert, H.: The MAP special
observing period, *Bull. Amer. Meteor. Soc.*, 82, 433–462, doi:10.1175/1520-0477(2001)082<0433:TMSOP>2.3.CO;2, 2001.
- Bougeault, P. et al.: The atmospheric momentum budget over a major mountain range : first results of the PYREX field program, *Ann.
Geophys.*, 11, 395–418, 1993.
- 475 Chen, F. and Dudhia, J.: Coupling an advanced land surface-hydrology model with the Penn State-NCAR MM5 modeling system. Part I:
Model implementation and sensitivity, *Mon. Wea. Rev.*, 129, 569–585, 2001.
- Chou, M. D. and Suarez, M. J.: An efficient thermal infrared radiation parameterization for use in general circulation models., NASA Tech.
Memo., 104606, 85pp., 1994.
- Chouza, F., Reitebuch, O., Groß, S., Rahm, S., Freudenthaler, V., Toledano, C., and Weinzierl, B.: Retrieval of aerosol backscatter and
480 extinction from airborne coherent Doppler wind lidar measurements, *Atmos. Meas. Tech.*, 8, 2909–2926, doi:10.5194/amt-8-2909-2015,
2015.
- Dörnbrack, A. and Leutbecher, M.: Relevance of mountain waves for the formation of polar stratospheric clouds over Scandinavia: A 20 year
climatology, *Journal of Geophysical Research: Atmospheres*, 106, 1583–1593, doi:10.1029/2000JD900250, 2001.
- Dörnbrack, A., Leutbecher, M., Reichardt, J., Behrendt, A., Müller, K.-P., and Baumgarten, G.: Relevance of mountain wave cooling for the
485 formation of polar stratospheric clouds over Scandinavia: Mesoscale dynamics and observations for January 1997, *Journal of Geophysical
Research: Atmospheres*, 106, 1569–1581, doi:10.1029/2000JD900194, 2001.



- Dörnbrack, A., Birner, T., Fix, A., Flentje, H., Meister, A., Schmid, H., Browell, E. V., and Mahoney, M. J.: Evidence for inertia gravity waves forming polar stratospheric clouds over Scandinavia, *Journal of Geophysical Research: Atmospheres*, 107, SOL 30–1–SOL 30–18, doi:10.1029/2001JD000452, 2002.
- 490 Doyle, J. D., Shapiro, M. A., Jiang, Q., and Bartels, D. L.: Large-amplitude mountain wave breaking over Greenland, *J. Atmos. Sci.*, 62, 3106–3126, doi:10.1175/JAS3528.1, 2005.
- Durrán, D. R.: Mountain waves and downslope winds, *Meteor. Monogr.*, 23, 59–81, 1990.
- Durrán, D. R., Hills, M. O. G., and Blossey, N.: The dissipation of trapped lee waves. Part I: Leakage of inviscid waves into the Stratosphere, *J. Atmos. Sci.*, 72, 1569–1584, doi:10.1175/JAS-D-14-0238.1, 2015.
- 495 Ehard, B., Achtert, P., Dörnbrack, A., Gisinger, S., Gumbel, J., Khaplanov, M., Rapp, M., and Wagner, J. S.: Combination of lidar and model data for studying deep gravity wave propagation, *Mon. Wea. Rev.*, 144, 77–98, doi:10.1175/MWR-D-14-00405.1, 2016.
- Eliassen, A. and Palm, E.: On the transfer of energy in stationary mountain waves, *Geophys. Publ.*, 22(3), 1–23, 1960.
- Fenoglio-Marc, L., Scharroo, R., Annunziato, A., Mendoza, L., Becker, M., and Lillibridge, J.: Cyclone Xaver seen by geodetic observations, *Geophys. Res. Lett.*, 42, 9925–9932, doi:10.1002/2015GL065989, 2015.
- 500 Frehlich, R.: Estimation of velocity error for Doppler lidar measurements, *J. Atmos. Oceanic Technol.*, 18, 1628–1639, doi:10.1175/1520-0426(2001)018<1628:EVOEFD>2.0.CO;2, 2001.
- Fritts, D. C. and Alexander, M. J.: Gravity wave dynamics and effects in the middle atmosphere, *Rev. Geophys.*, doi:10.1029/2001RG000106, 2003.
- Fritts, D. C. et al.: The Deep Propagating Gravity Wave Experiment (DEEPWAVE): An airborne and ground-based exploration of gravity wave propagation and effects from their sources throughout the lower and middle atmosphere, *Bull. Amer. Meteor. Soc.*, doi:10.1175/BAMS-D-14-00269.1, 2016.
- 505 Giez, A., Mallaun, C., Zöger, M., Dörnbrack, A., and Schumann, U.: Comparison of static pressure from aircraft trailing cone measurements and numerical weather prediction analysis, *AIAA Aviation*, doi:10.2514/6.2016-3707, 2016.
- Groß, S., Wirth, M., Schäfler, A., Kaufmann, S., and Voigt, C.: Potential of airborne lidar measurements for cirrus cloud studies, *Atmos. Meas. Tech.*, 7, 2745–2755, doi:10.5194/amt-7-2745-2014, 2014.
- 510 Grubišić, V., Doyle, J. D., Kuettner, J., Dirks, R., Cohn, S. A., Pan, L. L., Mobbs, S., Smith, R. B., Whiteman, C. D., Czyzyk, S., Vosper, S., Weissmann, M., Haimov, S., De Wekker, S. F. J., and Chow, F. K.: The terrain-induced rotor experiment, *Bull. Amer. Meteor. Soc.*, 89, 1513–1533, doi:10.1175/2008BAMS2487.1, 2008.
- Hills, M. O. G., Durrán, D. R., and Blossey, N.: The dissipation of trapped lee waves. Part II: The relative importance of the boundary layer and the Stratosphere, *J. Atmos. Sci.*, 73, 943–955, doi:10.1175/JAS-D-15-0175.1, 2016.
- 515

**J. S. Wagner: GWLCYCLE I campaign**

21

- Holton, J. R. and Alexander, M. J.: Atmospheric sciences across the stratopause, chap. The role of waves in the transport circulation of the middle atmosphere, p. 342, American Geophysical Union, Washington, D. C., doi:10.1029/GM123p0021, 2000.
- Hong, S.-Y. and Lim, J.-O. J.: The WRF single-moment 6-class microphysics scheme (WSM6), *J. Korean Meteor. Soc.*, 42, 129–151, 2006.
- Jiang, J. H., Wu, D. L., Eckermann, S. D., and Ma, J.: Mountain waves in the middle atmosphere: Microwave limb sounder observations and analyses, *Adv. Space Res.*, 32, 801–806, doi:10.1016/S0273-1177(03)00402-2, 2003.
- 520
- Jiang, Q., Doyle, J. D., Reinecke, A., Smith, R. B., and Eckermann, S. D.: A modeling study of stratospheric waves over the southern Andes and Drake passage, *J. Atmos. Sci.*, 70, 1668–1689, doi:10.1175/JAS-D-12-0180.1, 2013.
- Kaifler, B., Kaifler, N., Ehard, B., Dörnbrack, A., Rapp, M., and Fritts, D.: Influences of source conditions on mountain wave penetration into the stratosphere and mesosphere, *Geophys. Res. Lett.*, 42, doi:10.1002/2015GL066465, 2015.
- 525
- Kain, J. S. and Fritsch, J. M.: A one-dimensional entraining/detraining plume model and its application in convective parameterization, *J. Atmos. Sci.*, 47, 2784–2802, 1990.
- Keller, T. L.: Implications of the hydrostatic assumption on atmospheric gravity waves, *J. Atmos. Sci.*, 51, 1915–1929, doi:10.1175/1520-0469(1994)051<1915:IOTHAO>2.0.CO;2, 1994.
- Kim, Y.-J., Eckermann, S., D., and Chun, H.-Y.: An overview of the past, present and future of gravity-wave drag parameterization for numerical climate and weather prediction models, *Atmosphere-Ocean*, 41, 65–98, doi:10.3137/ao.410105, 2003.
- 530
- Klemp, J. B., Dudhia, J., and Hassiotis, A. D.: An upper gravity-wave absorbing layer for NWP applications, *Mon. Wea. Rev.*, 136, 3987–4004, 2008.
- Köpp, F., Rahm, S., and Smalikho, I.: Characterization of aircraft wake vortices by 2- μ m pulsed doppler lidar, *J. Atmos. Oceanic Technol.*, 21, 194–206, 2003.
- 535
- Kruse, C. G. and Smith, R. B.: Gravity wave diagnostics and characteristics in mesoscale fields, *J. Atmos. Sci.*, 72, 4372–4392, doi:10.1175/JAS-D-15-0079.1, 2015.
- Leutbecher, M. and Volkert, H.: The propagation of mountain waves into the stratosphere: quantitative evaluation of three-dimensional simulations, *J. Atmos. Sci.*, 57, 3090–3108, doi:10.1175/1520-0469(2000)057<3090:TPOMWI>2.0.CO;2, 2000.
- Mallaun, C., Giez, A., and Baumann, R.: Calibration of 3-D wind measurements on a single-engine research aircraft, *Atmos. Meas. Tech.*, 8, 3177–3196, doi:10.5194/amt-8-3177-2015. ISSN 1867-1381, 2015.
- 540
- Mlawer, E. J., Taubman, S. J., Brown, P. D., Iacono, M. J., and Clough, S. A.: Radiative transfer for inhomogeneous atmospheres: RRTM, a validated correlated-k model for the longwave., *J. Geophys. Res.*, 102, 16 663–16 682, 1997.
- Müller, S., Hoor, P., Berkes, F., Bozem, H., Klingebiel, M., Reutter, P., Smit, H. G. J., Wendisch, M., Spichtinger, P., and Borrmann, S.: In situ detection of stratosphere-troposphere exchange of cirrus particles in the midlatitudes, *Geophys. Res. Lett.*, 42, 949–955, doi:10.1002/2014GL062556, 2015.
- 545



22

J. S. Wagner: GWLCYCLE I campaign

Nakanishi, M. and Niino, H.: Development of an improved turbulence closure model for the atmospheric boundary layer, *J. Met. Soc. Japan*, 87, 895–912, 2009.

Queney, P.: The problem of airflow over mountains: A summary of theoretical studies, *Bull. Amer. Meteor. Soc.*, 29, 16–27, 1948.

Rautenhaus, M., Bauer, G., and Dörnbrack, A.: A web service based tool to plan atmospheric research flights, *Geosci. Model Dev.*, 5, 55–71,
550 doi:10.5194/gmd-5-55-2012, 2012.

Schmugge, T. J., Abrams, M. J., Kahle, A. B., Yamaguchi, Y., and Fujisada, H.: Advanced spaceborne thermal emission and reflection radiometer (ASTER), *Remote Sensing for Agriculture, Ecosystems and Hydrology*, 4, doi:10.1117/12.469693, 2003.

Scorer, R. S.: Theory of waves in the lee of mountains, *Q. J. R. Meteorol. Soc.*, 75, 41–56, 1949.

Skamarock, W. C., Klemp, J. B., Dudhia, J., Gill, D. O., Barker, D. M., Duda, M. G., Huang, X.-Y., Wang, W., and Powers, J. G.: A description
555 of the Advanced Research WRF Version 3, NCAR technical note, Mesoscale and Microscale Meteorology Division, National Center for Atmospheric Research, Boulder, Colorado, USA, 2008.

Smalikho, I.: Techniques of wind vector estimation from data measured with a scanning coherent doppler lidar, *J. Atmos. Oceanic Technol.*, 20, 276–291, 2003.

Smith, R. B., Skubis, S., Doyle, J. D., Broad, A. S., Kiemle, C., and Volkert, H.: Mountain waves over Mont Blanc: Influence of a stagnant
560 boundary layer, *J. Atmos. Sci.*, 59, 2073–2092, doi:10.1175/1520-0469(2002)059<2073:MWOMBI>2.0.CO;2, 2002.

Smith, R. B., Woods, B. K., Jensen, J., Cooper, W. A., Doyle, J. D., Jiang, Q., and Grubišić, V.: Mountain waves entering the stratosphere, *J. Atmos. Sci.*, 65, 2543–2562, 2008.

Weissmann, M., Busen, R., Dörnbrack, A., Rahm, S., and Reitebuch, O.: Targeted observations with an airborne wind lidar, *J. Atmos. Oceanic Technol.*, 22, 1706–1719, 2005.

565 Witschas, B., Rahm, S., Wagner, J. S., and Dörnbrack, A.: Airborne coherent Doppler wind lidar measurements of vertical and horizontal wind speeds for the investigation of gravity waves, in: *Coherent Laser Radar Conference*, 2016.



J. S. Wagner: GWLCYCLE I campaign

23

Table 1. Overview of intensive observation periods (IOP) during GW-LCYCLE I. Start and end times of research flights are indicated in UTC. For each flight the number of airborne lidar profiles in both nadir and scanning mode (see section 2.2) and the corresponding coverage of useable data in percentage is shown. Radiosondes were released at Andenes (A), Esrange (E), Kiruna (K) and Sodankylä (S) (see Fig. 1).

IOP	Date	Research flights		Airborne lidar profiles		Radiosondes				Description
		Start	End	Nadir	Scan	A	E	K	S	
1	03.12.2013	09:13	11:26	2379 (41.93%)	6 (26.24%)	9	9	7	10	Mountain wave event
		13:25	16:22	1328 (39.24%)	100 (67.56%)					
2	05.12.2013	08:33	11:48	7222 (36.24%)	21 (36.85%)	-	-	-	-	Storm Xaver
3	09.12.2013	12:08	14:58	2408 (7.84%)	-	-	-	-	-	Trace gas/pollution event
4	11.12.2013	-	-	-	-	6	7	7	11	Mountain wave event
5	13.12.2013	06:10	09:37	2250 (38.33%)	68 (53.72%)	5	5	8	8	Mountain wave event
		12:19	15:24	2305 (47.97%)	39 (44.19%)					

Table 2. Overview of real-case simulations for cases with full (CTRL), smoothed (SMTOPO) and without (NOTOPO) topography and cases with a flat water surface (OCEAN). Idealised simulations are performed for hydrostatic (HYDRO) and trapped waves (TRAPPED) by flow over a Witch of Agnesi mountain with constant horizontal wind speed. The stratification is given by constant Brunt-Vaisala frequencies N in the planetary boundary layer (PBL), Troposphere and Stratosphere.

Case	Type	Topography D1	Topography D2	Topography D3	Landuse
CTRL	real-case	full	full	full	land-ocean
SMTOPO	real-case	full	smoothed	smoothed	land-ocean
NOTOPO	real-case	flat	flat	flat	land-ocean
OCEAN	real-case	flat	flat	flat	ocean

Case	Type	N PBL (s^{-1})	N Troposphere (s^{-1})	N Stratosphere (s^{-1})	Wind speed ($m s^{-1}$)
HYDRO	idealised	0.01	0.01	0.01	10
TRAPPED	idealised	0.016	0.0045	0.02	20



Table 3. Correlation coefficients between airborne in-situ and lidar observations and numerical models for potential temperature Θ , horizontal wind speed U , vertical wind speed w and wind direction dd along all flight legs during both IOP1 and IOP5 (numbers in bold).

Model	In-situ Θ	In-situ U	In-situ w	In-situ dd	Lidar U	Lidar w
CTRL D3	0.992 0.996	0.877 0.963	0.154 0.343	0.892 0.868	0.755 0.917	0.242 0.408
CTRL D2	0.993 0.996	0.872 0.964	0.169 0.361	0.883 0.858	0.735 0.913	0.300 0.417
CTRL D1	0.993 0.997	0.872 0.964	0.156 0.213	0.868 0.858	0.712 0.916	0.205 0.218
ECMWF	0.992 0.998	0.891 0.967	0.116 0.076	0.858 0.897	0.414 0.882	-0.064 -0.092



J. S. Wagner: GWLCYCLE I campaign

25

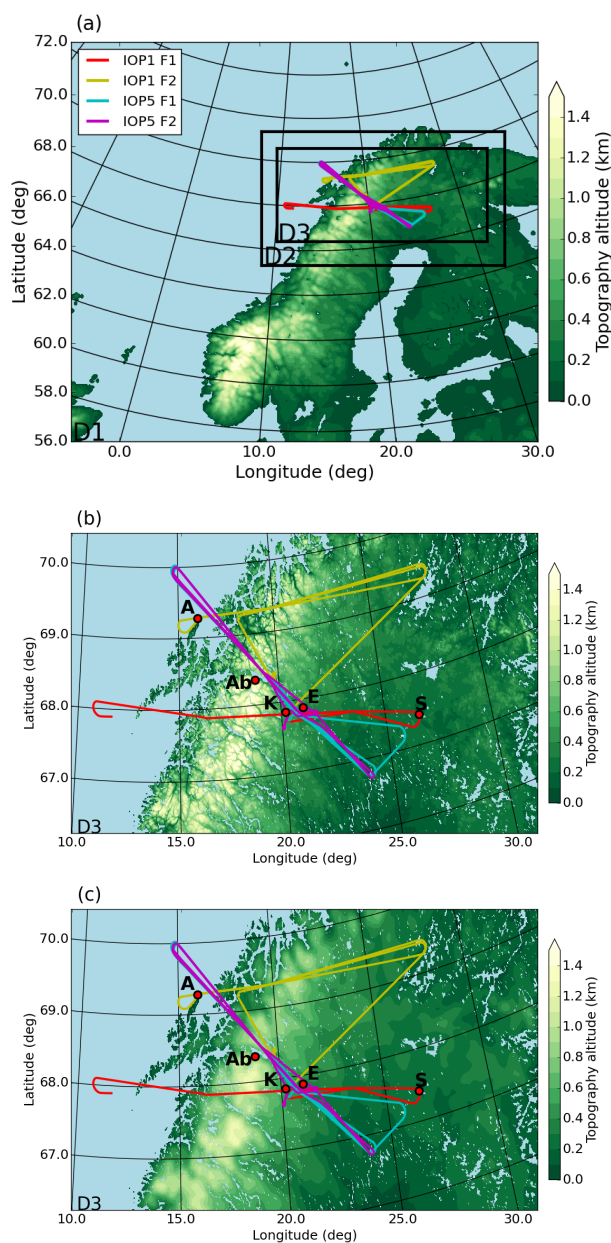


Figure 1. Topography map of Scandinavia and location of the GW-LCYCLE I campaign. The coloured lines indicate DLR Falcon flighttracks during IOP1 and IOP5. In (a) the shown region and the black boxes mark the modelling domains for mesoscale WRF simulations with horizontal grid sizes Δx of 7.2 km (D1), 2.4 km (D2) and 0.8 km (D3), respectively. The topography of domain D3 is shown in (b) for the CTRL and in (c) for the SMTPO simulation (see Table 2). The red dots mark the position of Andenes (A), Abisko (Ab), Kiruna (K), Esrange (E) and Sodankylä (S).

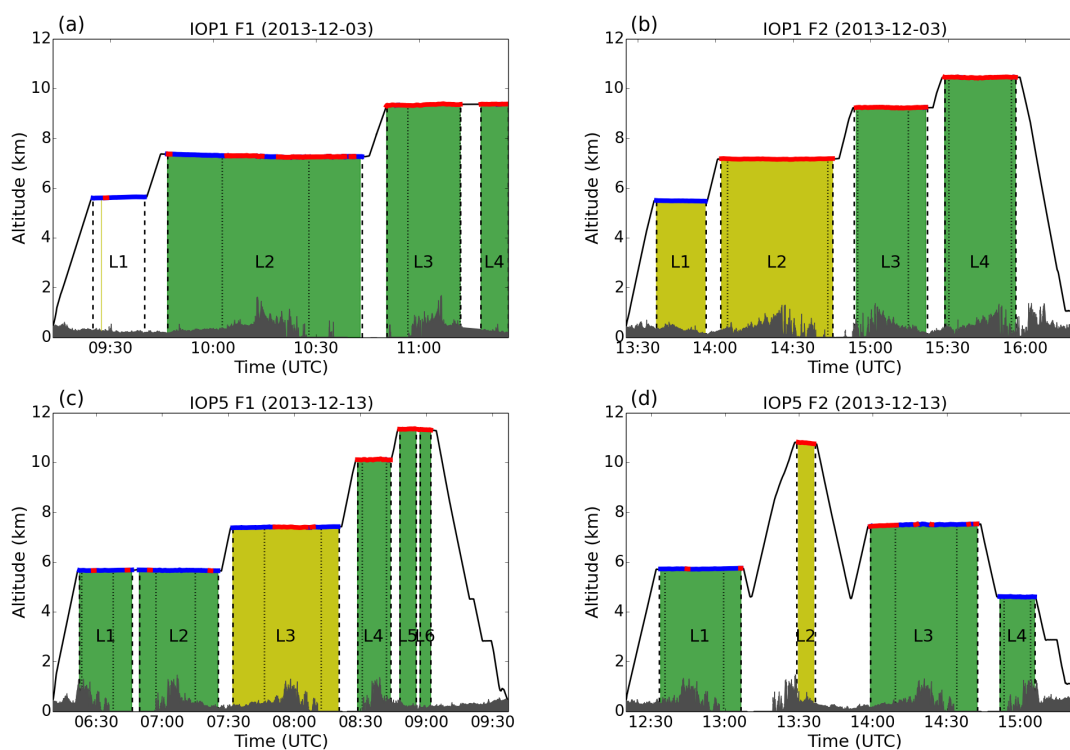


Figure 2. Flight legs and altitudes of the four research flights during (a) and (b) IOP1 and (c) and (d) IOP5. The yellow and green shaded areas indicate regions where the airborne lidar operated in scanning and nadir pointing mode, respectively. Blue and red thick lines indicate respective flight altitudes below and above the tropopause, which was determined by in-situ trace gas measurements of N_2O with a threshold value of 326.6 ppbv (see section 2.2). The black dashed and dotted lines mark flight legs used for data analysis and indicate complete flight legs and leg sections limited to mountain regions, respectively. The topography along the flight tracks is based on the ASTER data set.



J. S. Wagner: GWLCYCLE I campaign

27

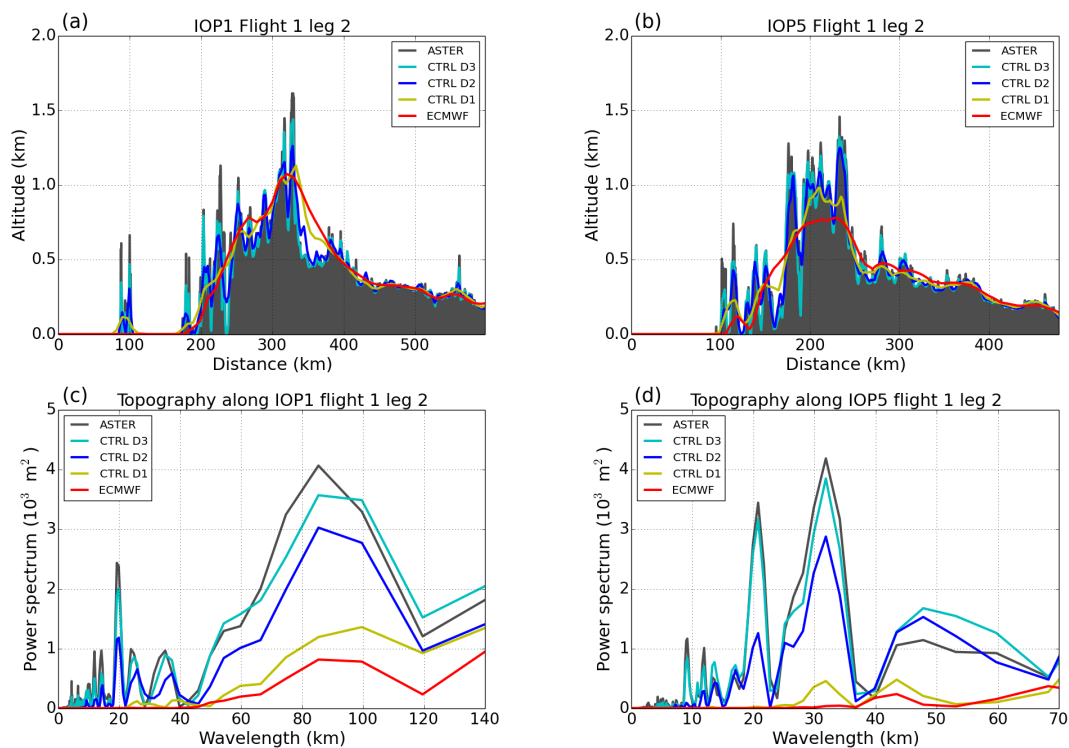


Figure 3. Comparison of topography along leg 2 of flight 1 during (a) and (c) IOP1 and (b) and (d) IOP5 for the high resolution ASTER data set, CTRL and ECMWF topographies. In (c) and (d) powerspectra of the topographies in (a) and (b) are shown.

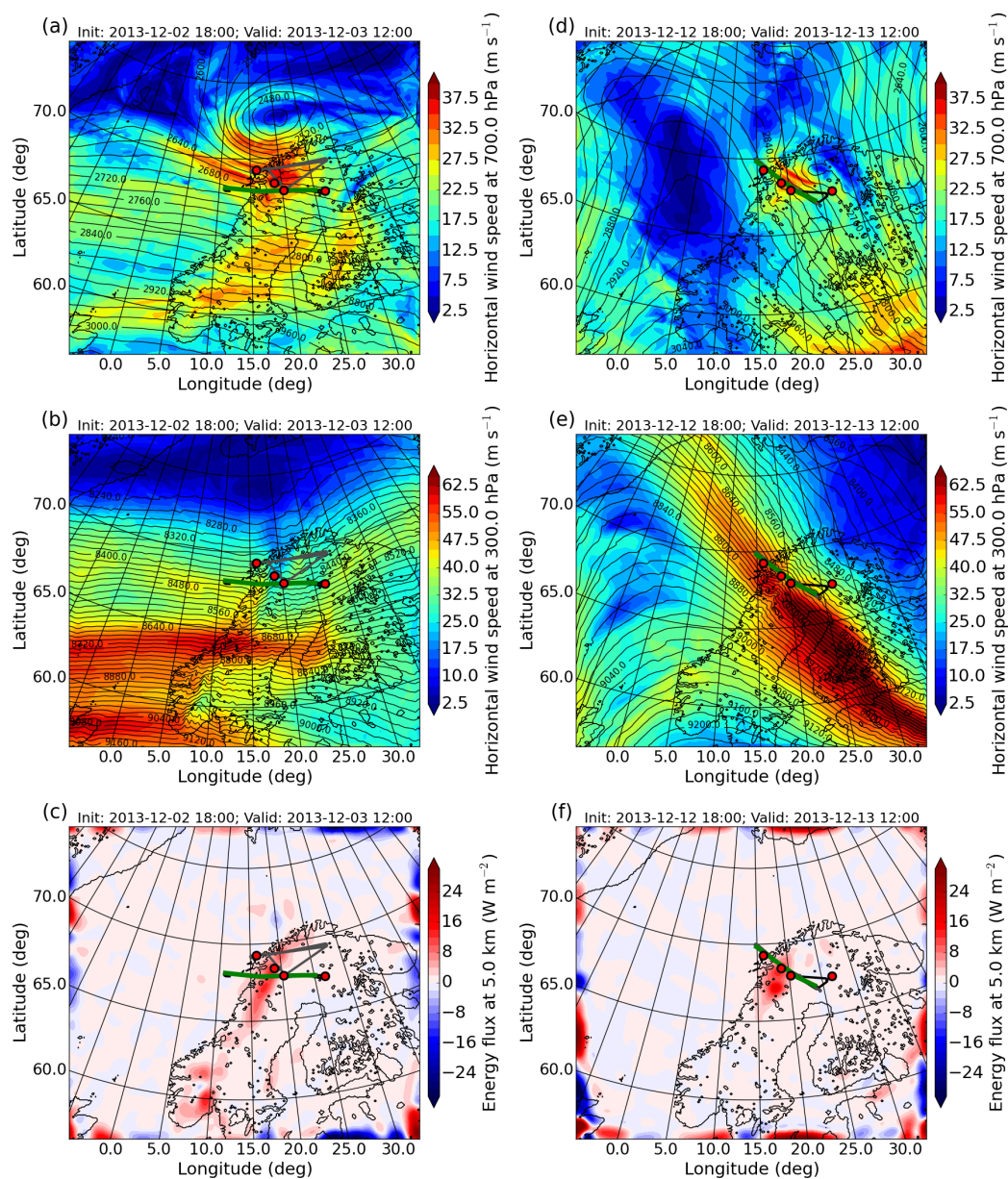


Figure 4. Synoptic situation and respective flight tracks during (a) to (c) IOP1 and (d) to (f) IOP5. Shown are CTRL D1 ($\Delta x = 7.2$ km) horizontal wind speed and geopotential height at (a) and (d) 700 hPa and (b) and (e) 300 hPa and GW induced vertical energy fluxes at 5 km altitude in (c) and (f). The red dots mark the locations of Andenes (A), Abisko (Ab), Kiruna (K) and Sodankylä (S) (cf. Fig. 1). The first and second flight of IOP1 and IOP5 are plotted with black and grey lines, respectively. The chosen times at 12 UTC, 3 December and 12 UTC, 13 December are valid between the respective two research flights (cf. Table 1 and Fig. 2).



J. S. Wagner: GWLCYCLE I campaign

29

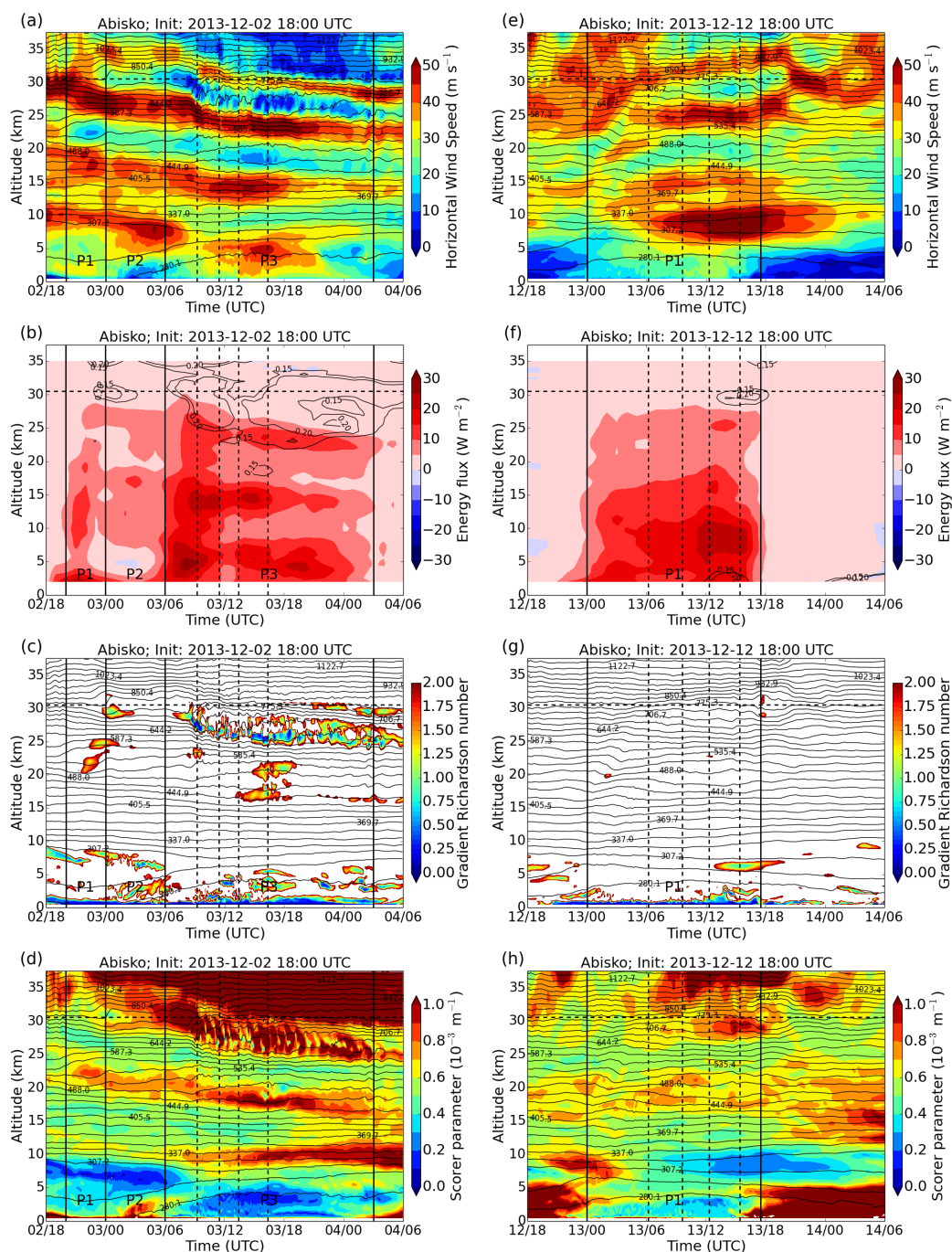


Figure 5. Time height sections of CTRL D2 simulations at Abisko (68° N, 19° E) during (a) to (d) IOP1 and (e) to (h) IOP5 for horizontal wind speed, vertical energy flux, gradient Richardson number and Scorer parameter. The vertical solid and dashed lines mark the different mountain wave phases and periods of research flights. The dashed horizontal line indicates the height of the sponge layer at the model top. Thin black contour lines mark the nonlinearity ratio (NLR) of Kruse and Smith (2015) in (b) and (f) and isentropes in the remaining figures.

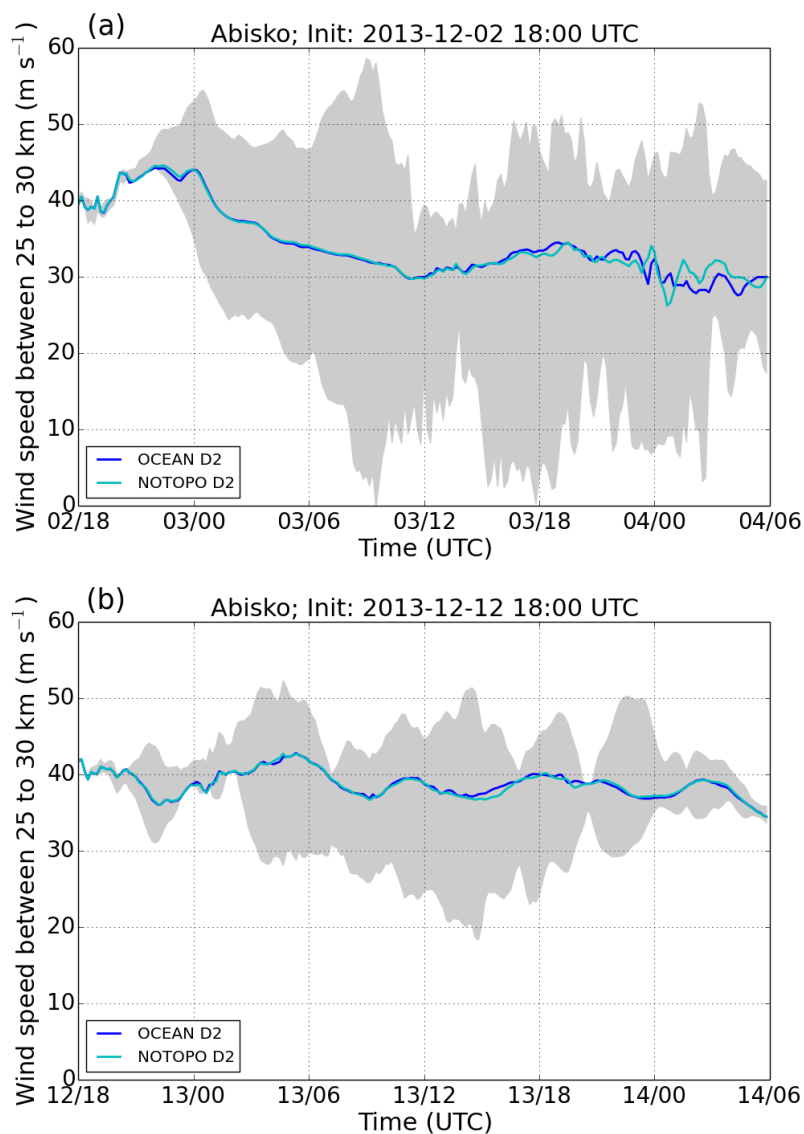


Figure 6. Time series of background horizontal wind speed averaged between 25 to 30 km (solid lines) of the OCEAN and NOTOPO simulation at Abisko (68° N, 19° E) for (a) IOP1 and (b) IOP5. The grey shaded area marks the range of minimum and maximum wind speed perturbations (mountain wave induced) at 25 to 30 km determined by subtracting OCEAN from CTRL simulation fields. All data is based on domain D2.

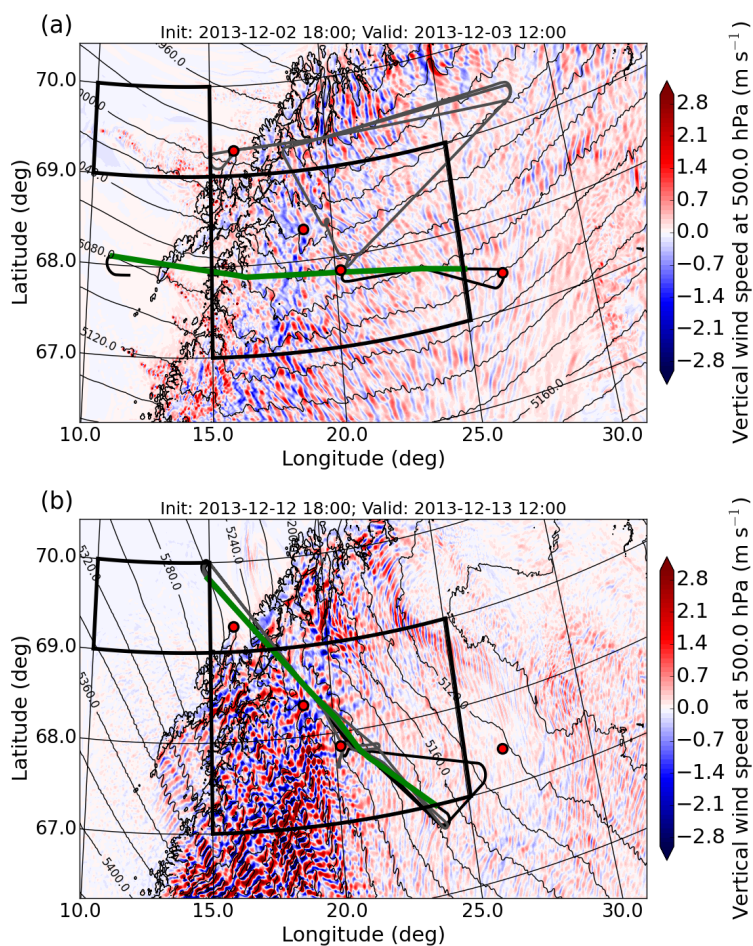


Figure 7. CTRL D3 ($\Delta x = 0.8$ km) vertical wind speed at 500 hPa during (a) IOP1 and (b) IOP5. The red dots mark the locations of Andenes, Abisko, Kiruna and Sodankylä (cf. Fig. 1). The first and second flights of IOP1 and IOP5 are plotted with black and grey lines, respectively. The thick green line marks the second flight leg of the corresponding first research flight. Black boxes show regions for the computation of vertical profiles in an upstream (small box) and mountain (large box) region (see Fig. 8).

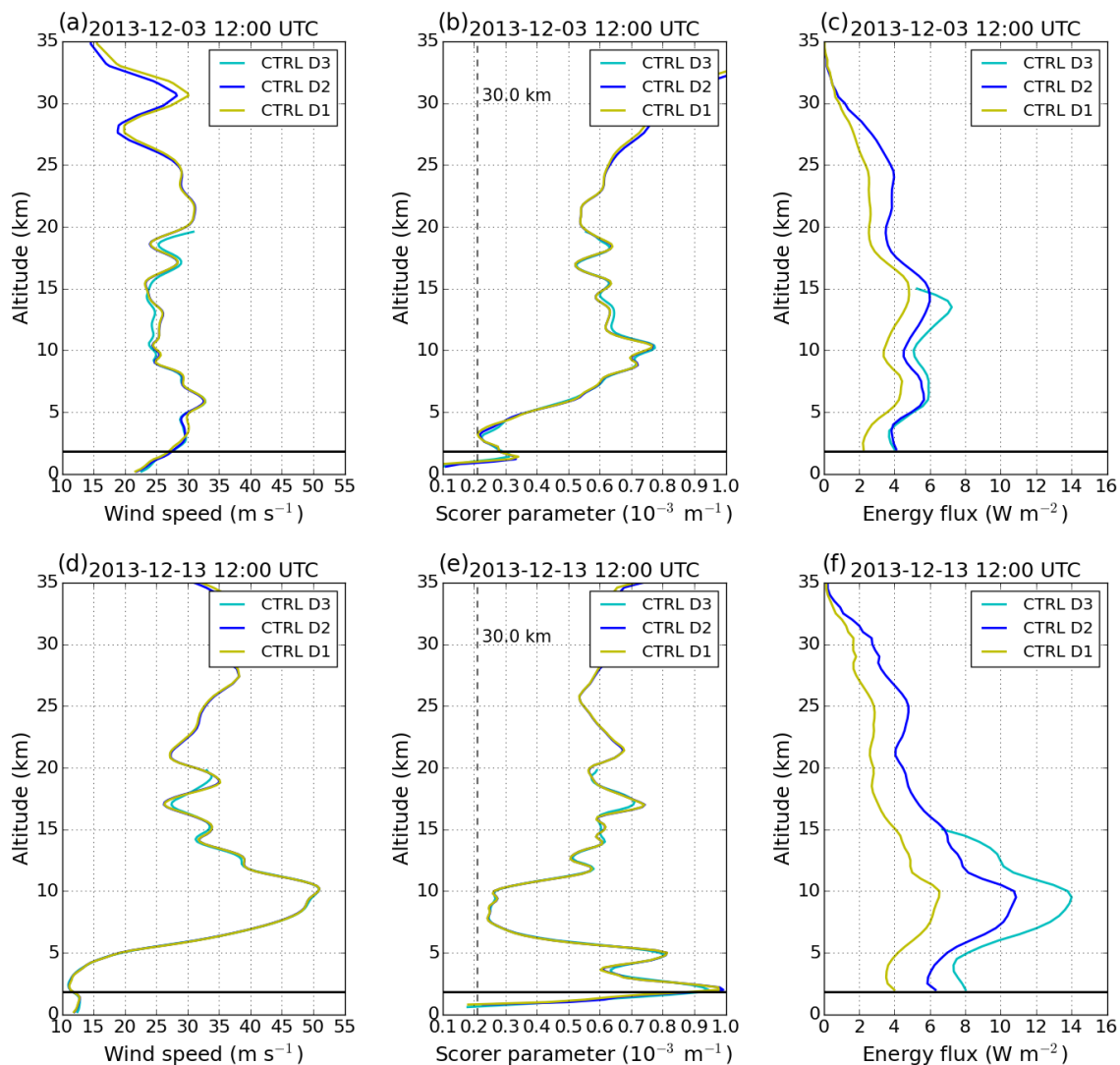


Figure 8. Area averaged vertical profiles during (a) to (c) IOP1 and (e) to (f) IOP5. Cross mountain horizontal wind speed (from a direction of 300°) and Scorer parameter are averaged over the upstream area from 69°N to 70°N and 10°E to 15°E , while vertical energy fluxes are averaged over the mountain area within 67°N to 69°N and 15°E to 25°E (see black boxes in Fig. 7). The thick horizontal black line marks the maximum mountain peak height within the mountain box and the dashed vertical black line in (b) and (e) indicates a horizontal wavelength of 30 km.



J. S. Wagner: GWLCYCLE I campaign

33

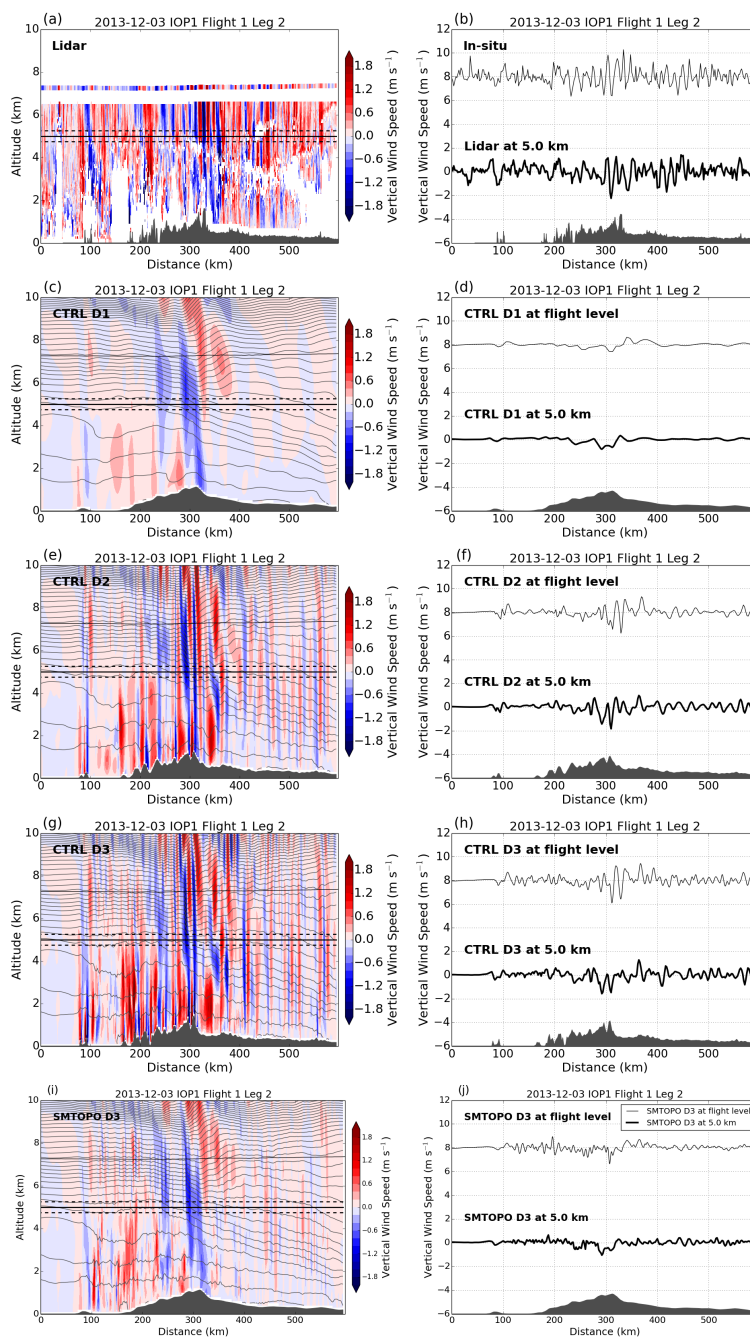


Figure 9. Cross sections for vertical velocity of flight 1, leg 2 during IOP1 for (a) and (b) lidar and in-situ measurements, (c) and (d) CTRL D1, (e) and (f) CTRL D2, (g) and (h) CTRL D3 and (i) and (j) SMTOP0 D3 simulations. In the left panels vertical wind is shown with coloured contours and potential temperature with contour lines. The right panels show vertical velocities at flight level (see thin black line in the left panels) and at 5 km altitude averaged over a layer ± 250 m (see thick black solid and dashed lines in the left panels). Note that the flight level data are shifted by 8 m s^{-1} in the right panels.

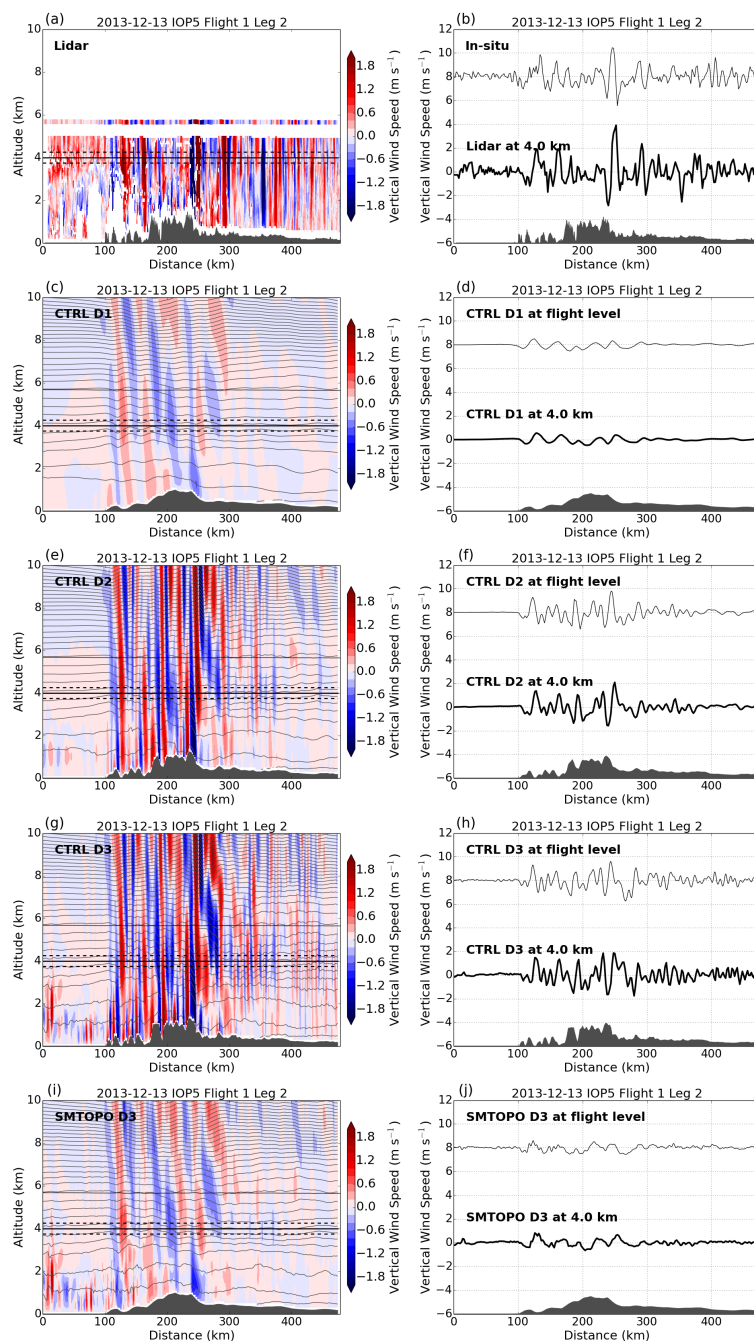


Figure 10. As in Fig. 9, but for flight 1, leg 2, during IOP5. Vertical velocities are shown at flight level and at 4 km altitude in the right panels.



J. S. Wagner: GWLCYCLE I campaign

35

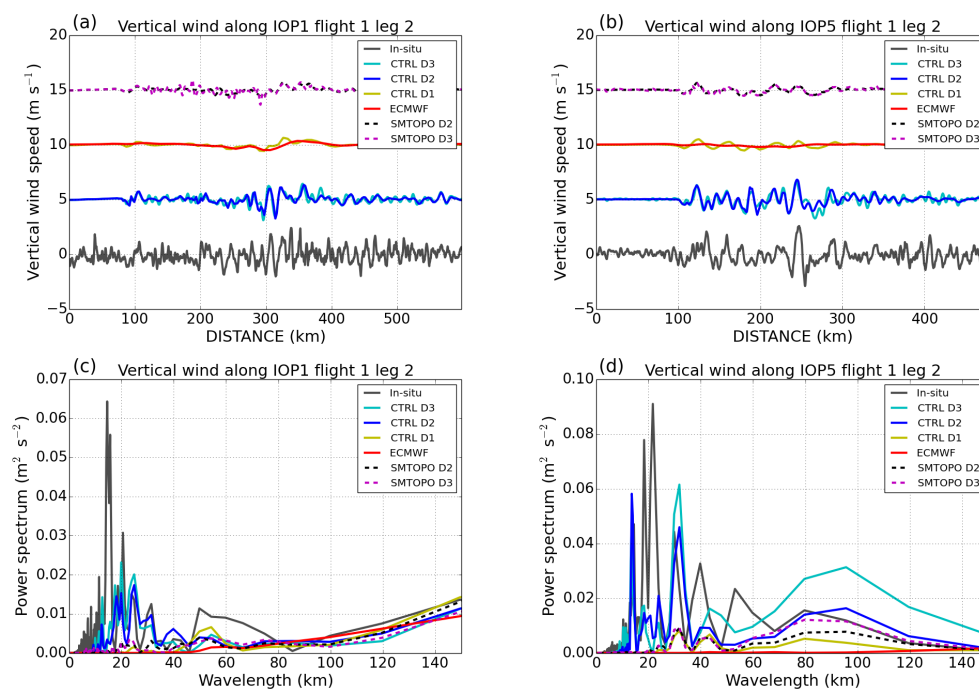


Figure 11. As in Fig. 3, but for vertical velocity at flight level. To improve readability, vertical wind speeds are shifted by 5 m s⁻¹ in (a) and (b).

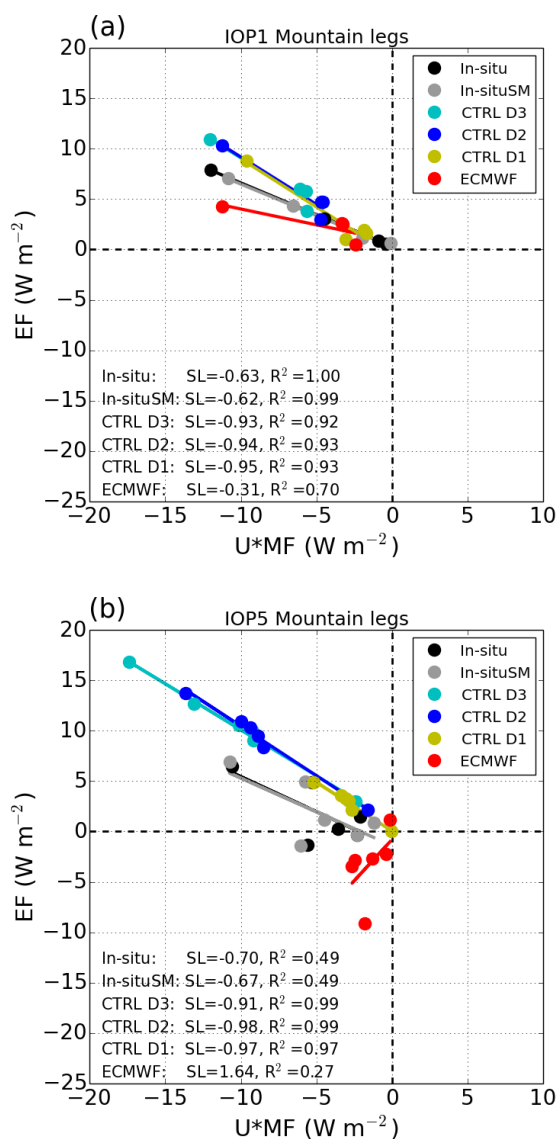


Figure 12. Leg-integrated Eliassen-Palm relation between energy flux (EF) and momentum flux (MF) multiplied by leg averaged horizontal wind speed U along all flight legs during (a) IOP1 and (b) IOP5 for observed and simulated data at flight level. Smoothed in-situ data including all waves with wavelengths larger than 15 km are marked with gray dots (In-situSM). The solid lines mark linear regressions with slopes (SL) and correlation coefficients (R^2) indicated in the lower left of the figure. To exclude effects of non-orographic GWs only data directly over the mountains are utilized (see Fig. 2 for leg locations).



J. S. Wagner: GWLCYCLE I campaign

37

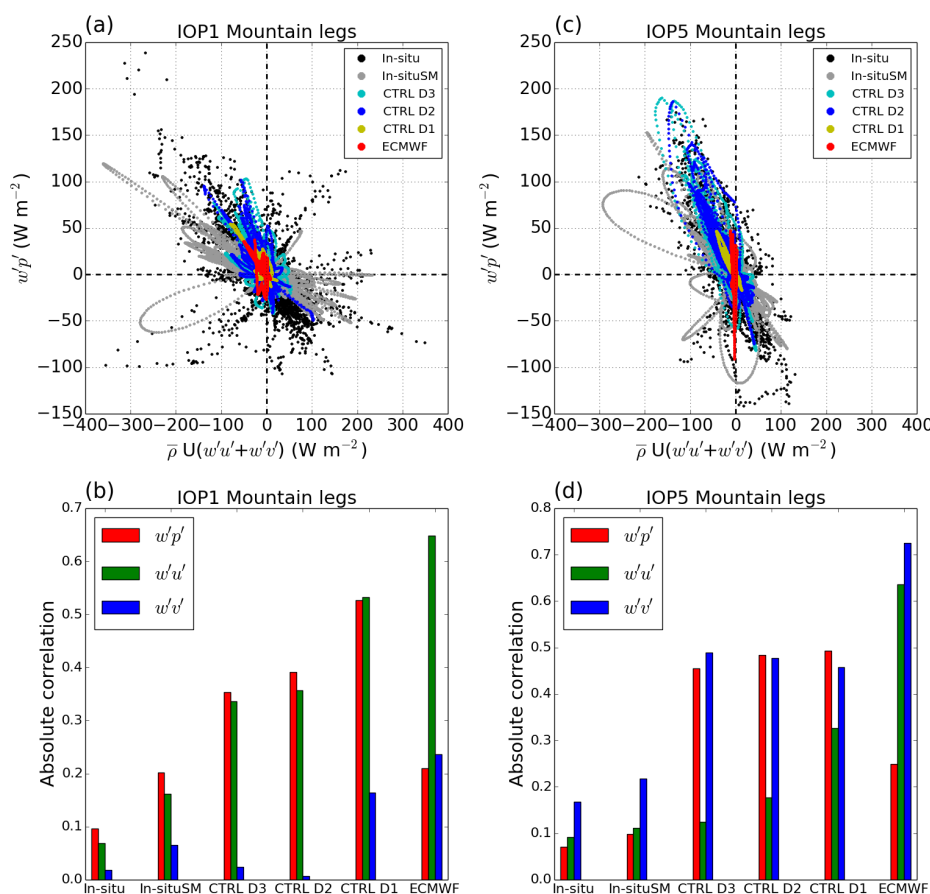


Figure 13. Pointwise correlation of energy and momentum fluxes along all flight legs during (a) IOP1 and (c) IOP5 for observed and simulated data at flight level. Smoothed in-situ data including all waves with wavelengths larger than 15 km are marked with gray dots (In-situSM). In (b) and (d) absolute values of correlation coefficients are shown for perturbation variables w' (vertical wind), p' (pressure), u' (zonal wind) and v' (meridional wind) at flight level for IOP1 and IOP5, respectively.

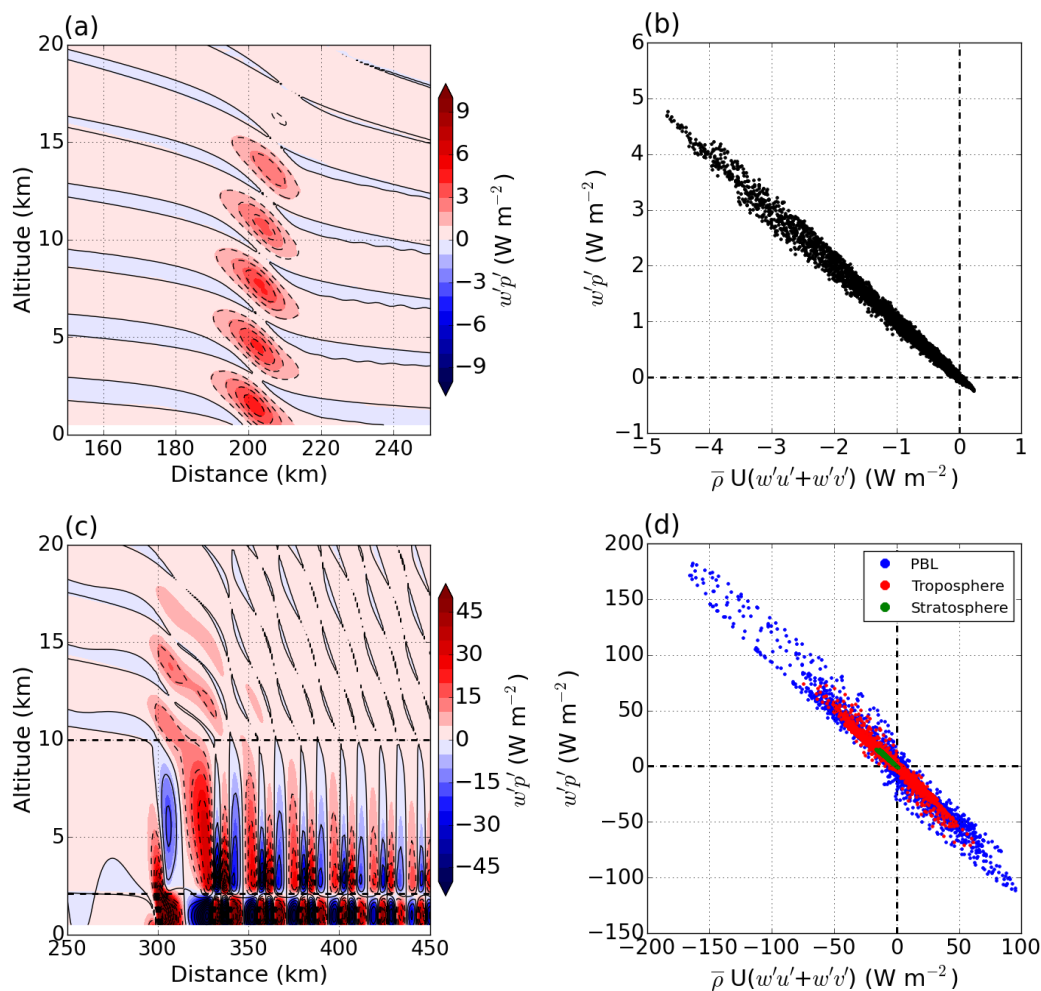


Figure 14. Relation between EF and MF in idealised simulations of (a) and (b) hydrostatic mountain waves (HYDRO) and (c) and (d) trapped lee waves (TRAPPED). In (a) and (c) EF (coloured contours) and MF (black contour lines, negative values dashed) are shown after 10 h of simulation. In (b) and (c) the pointwise Eliassen-Palm relation between EF and MF is plotted for all data points.



J. S. Wagner: GWLCYCLE I campaign

39

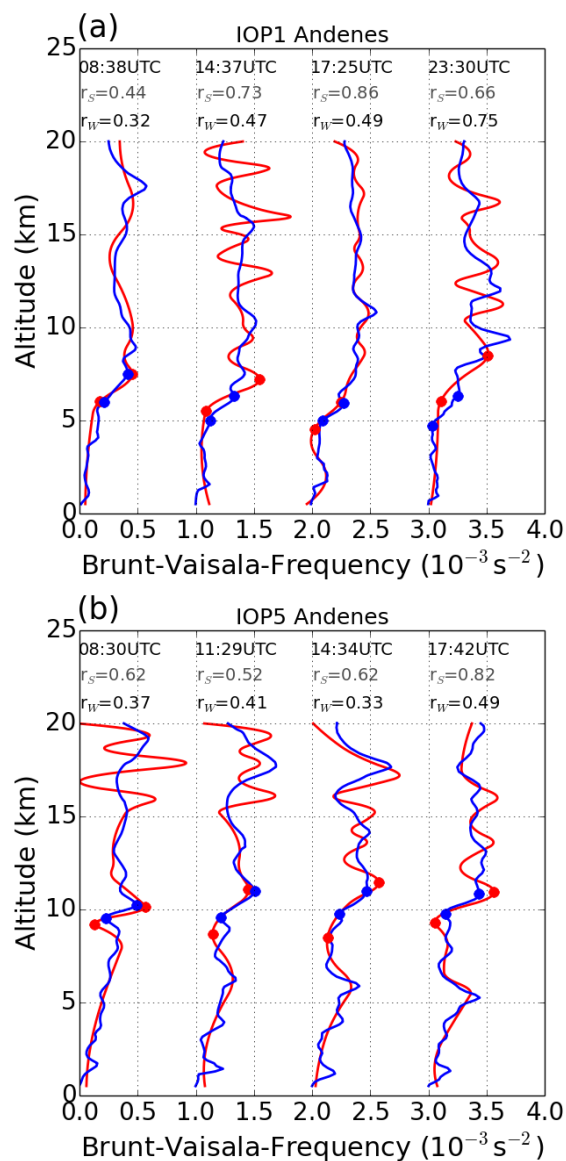


Figure 15. Brunt-Vaisala frequency profiles obtained from soundings launched at Andenes during (a) IOP1 and (b) IOP5. The red and blue lines show observed and CTRL D2 data, respectively. The jump in atmospheric stability at the tropopause is marked with dots. Launch times and wave reflection coefficients at the tropopause for soundings (r_s) and WRF (r_w) are indicated at the top of each profile. Profiles are shifted by 10^{-3} s^{-2} on the x-axis.

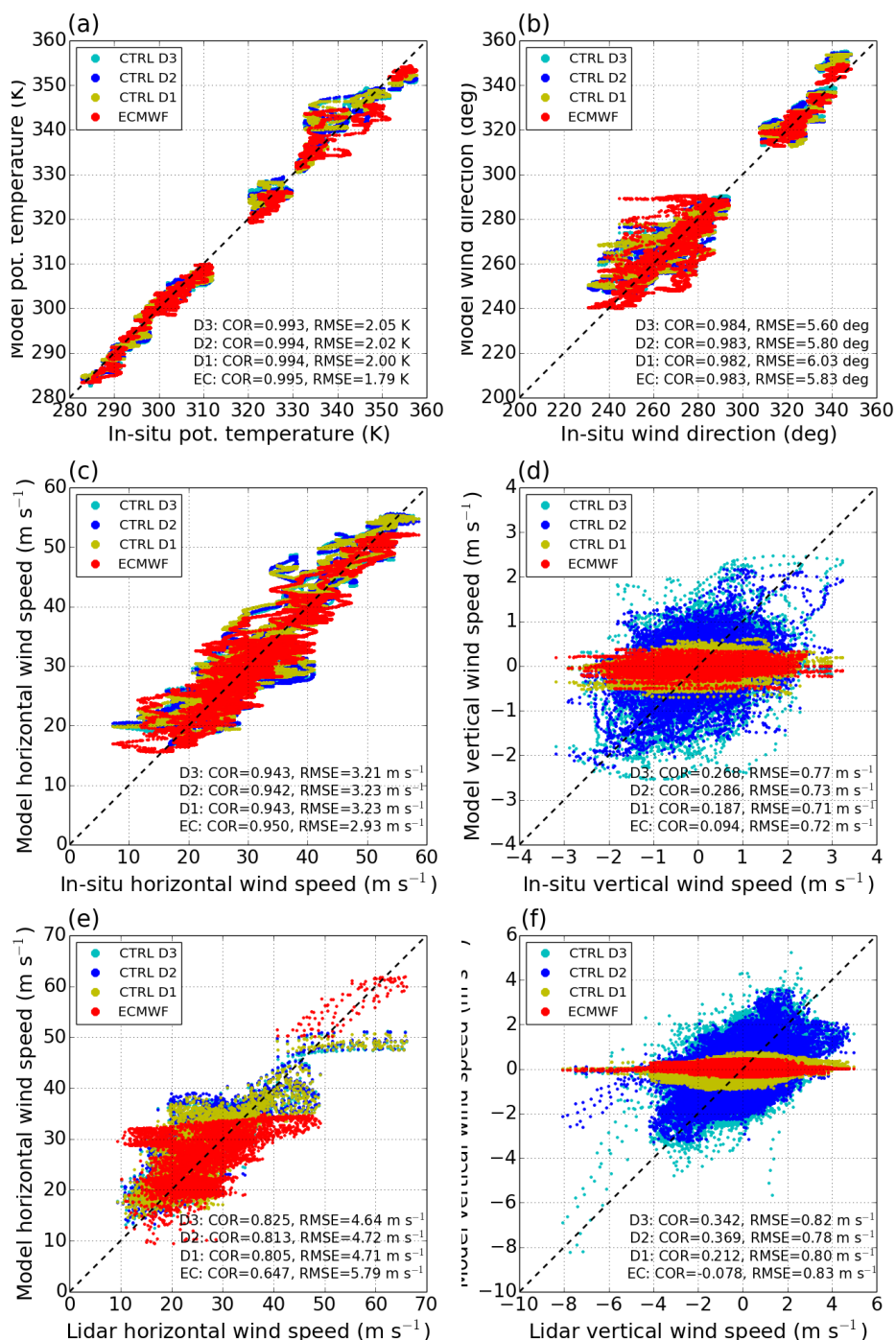


Figure 16. Correlation between in-situ and simulated (a) potential temperature, (b) wind direction, (c) horizontal and (d) vertical wind speed at flight level along all flight legs during IOP1 and IOP5. The correlation between simulations and lidar observations is shown in (e) for horizontal and in (f) for vertical wind speed along all lidar cross sections during IOP1 and IOP5. The identity line is marked with the dashed line. Correlation coefficients (COR) and root mean square errors (RMSE) are shown on the bottom of each figure.

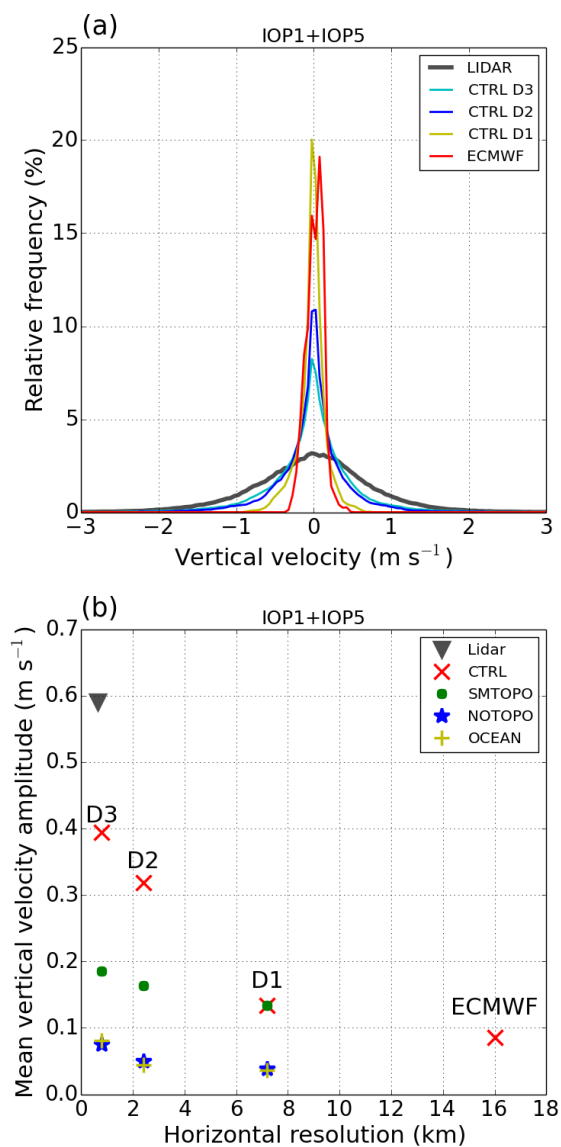


Figure 17. Lidar and model vertical velocity distribution (a) and mean vertical velocity amplitude in dependence of horizontal model grid resolution (b) for all lidar nadir pointing flight legs during both IOP1 and IOP5 (cf. Fig 2).